Available online at www.sciencedirect.com
SCIENCE DIRECT®
Journal of Solid State Chemistry 177 (2004) 3156–3173
JOURNAL OF SOLID STATE CHEMISTRY
http://elsevier.com/locate/jssc

Crystal structures and ionic conductivities of ternary derivatives of the silver and copper monohalides—II: ordered phases within the $(AgX)_x$–$(MX)_{1-x}$ and $(CuX)_x$–$(MX)_{1-x}$ (M = K, Rb and Cs; X = Cl, Br and I) systems

S. Hull[a,*] and P. Berastegui[b]

[a] *Rutherford Appleton Laboratory, The ISIS Facility, Oxfordshire, Chilton, Didcot, Oxon OX11 0QX, UK*
[b] *Arrhenius Laboratory, Stockholm University, S-106 91 Stockholm, Sweden*

Received 15 March 2004; received in revised form 4 May 2004; accepted 8 May 2004

Available online 15 July 2004

Abstract

The crystal structures of 23 ternary phases present in the systems $(AX)_x$–$(MX)_{1-x}$ (A = Ag, Cu; M = K, Rb and Cs; X = Cl, Br and I) have been determined and/or refined using X-ray and neutron diffraction studies of powder samples. A total of 11 $x = 0.333$ phases of stoichiometry M_2AX_3 are found (Rb_2AgCl_3, Cs_2AgCl_3, Rb_2AgBr_3, Cs_2AgBr_3, K_2AgI_3, Rb_2AgI_3, Cs_2AgI_3, K_2CuCl_3, K_2CuBr_3, Rb_2CuBr_3 and Rb_2CuCl_3) which crystallize in one of two closely related crystal structures with space group *Pnma*. The $x = 0.4$ composition is characterized by three compounds $Cs_3Cu_2X_5$ (X = Cl, Br, I) which all adopt space group *Pnma*, whilst the $x = 0.5$ case comprises the two compounds $CsAgCl_2$ and $CsAgBr_2$, which possess space group *Cmcm*. The latter undergo phase transitions at 408(5) and 413(8) K, respectively, to higher symmetry structures in space group $P4/nmm$. Five $x = 0.667$ compounds of stoichiometry MCu_2X_3 have been identified ($CsCu_2Cl_3$, $CsCu_2Br_3$, $CsCu_2I_3$, $RbCu_2Br_3$, and $RbCu_2I_3$). Together with $CsAg_2I_3$, these form a family of compounds, which crystallize in one of two closely related structures (space group *Pbnm* or *Cmcm*). Impedance spectroscopy measurements indicate that all the above-mentioned compounds have relatively low values of ionic conductivity ($\sigma < 10^{-4}\,\Omega^{-1}\,cm^{-1}$ at room temperature). Contrary to previous reports, no evidence of high conductivity phases of composition $CsCu_9Br_{10}$ and $CsCu_9I_{10}$ was obtained during high-temperature powder neutron diffraction studies. Some general remarks concerning the structural properties of these systems are given, together with a discussion of the influence of the M^+ cations on the ionic conductivity. Finally, the structural information for all the ambient temperature phases has been used to derive improved bond valence parameters for Ag–X and Cu–X bonds.

Keywords: Superionic conduction; Ag^+ diffusion; Cu^+ diffusion; Neutron diffraction; Impedance spectroscopy; Bond valence methods

1. Introduction

At elevated temperatures the compounds AgI, CuBr and CuI are some of the best known examples of superionic conductors [1]. On increasing temperature they undergo first-order solid–solid transitions to phases characterized by liquid-like values of the ionic conductivity (typically $\sigma \sim 1\,\Omega^{-1}\,cm^{-1}$, see Ref. [2] and references therein). It is now well established that these superionic phases can be described by rapid jump diffusion of the Ag^+/Cu^+ between the interstices formed by an essentially immobile anion sublattice (for a recent review, see Ref. [3]). The latter can be body centered cubic (e.g., α-AgI [4,5]), face centered cubic (e.g., α-CuI [6,7]) or hexagonal close packed (e.g., β-CuBr [8]).

The fundamental issue within the field of superionic conductors is to explain why AgI, CuBr and CuI display high ionic conductivities whilst other binary compounds (such as NaCl, LiI, or the other Ag^+ and Cu^+ halides) do not. On simple intuitive grounds, a number of plausible factors are likely to be influential, including the crystal structure and the properties (size,

*Corresponding author. Fax: +44-1235-445720.
E-mail address: s.hull@rl.ac.uk (S. Hull).

0022-4596/$ - see front matter © 2004 Elsevier Inc. All rights reserved.
doi:10.1016/j.jssc.2004.05.004

mass, polarizability, etc.) of the constituent ions (both mobile and immobile species). However, the relative importance of any one of these factors in promoting superionic behavior is difficult to assess, owing to the relatively small number of known superionic phases and the inherent inter-relationship between the individual factors. However, two approaches can be used to address this issue. The first is the use of high pressure to promote structural transitions to phases which are superionic (as in the case of CuCl-III [9]) and allow the superionic behavior within different structures of the same compound to be investigated (as in the cases of AgI [10] and CuI [7]). The second is the use of chemical doping of the binary compounds to produce ternary phases. Clearly, the addition of a third ionic species adds complexity but, using careful crystallographic and transport studies of a wide range of related ternary compounds, it is possible to extract important information concerning the influence of factors such as the crystal structure on the ionic diffusion mechanisms. In this vein, the authors are pursuing a comprehensive study of the crystal structures and ionic conductivities of ternary derivatives of the AgX and CuX (X = Cl, Br, I) compounds (see, for example, Refs. [11–15]).

The possibility that some ternary derivatives of the AgX and CuX compounds formed by the addition of monovalent M^+ cations (M = K, Rb, Cs) might possess similar (or even higher) ionic conductivities has motivated several studies of the various $(AgX)_x$–$(MX)_{1-x}$ and $(CuX)_x$–$(MX)_{1-x}$ phase diagrams and conductivity measurements of the observed phases [16–22]. It is generally accepted that the M^+ cations are immobile and do not directly contribute to the measured ionic conductivity [16]. However, as discussed previously [1], these dopants may play an important role in either promoting or hindering superionic behavior by modifying the structure of the anion sublattice. Specifically, in attempting to adopt their preferred (higher) co-ordination within the anion array, the addition of M^+ may produce a greater degree of face-sharing of the X^- polyhedra through which the Ag^+/Cu^+ can diffuse. Clearly, to assess these rather speculative remarks it is necessary to perform a detailed investigation of the crystal structures and ionic conductivities of the ternary compounds found within the $(AgX)_x$–$(MX)_{1-x}$ and $(CuX)_x$–$(MX)_{1-x}$ systems. This paper forms the second part of this comprehensive study. The three compounds of composition $x = 0.8$ ($RbAg_4I_5$, KAg_4I_5 and KCu_4I_5) are all superionic phases and have been discussed in the previous publication [15]. Indeed, $RbAg_4I_5$ and KAg_4I_5 have exceptionally high ionic conductivities at ambient temperature ($\sigma = 0.21(6)$ and $0.08(5)\,\Omega^{-1}\,cm^{-1}$, respectively [15]). Whilst a number of issues prohibit their commercial exploitation within solid state devices, including the high cost of silver, it is important from a fundamental point-of-view to examine how the superionic properties are enhanced by M^+ doping to form $RbAg_4I_5$ and KAg_4I_5. This question will be approached in Section 4, but a comprehensive investigation of this issue will be deferred to a future publication devoted to bond valence and molecular dynamics simulations. In preparation for the former, bond valence parameters for the six Ag–X and Cu–X bonds are derived and presented here.

2. Experimental

The samples used in this work were prepared under a variety of different conditions, as summarized in Table 1. Solid state reaction of the corresponding stoichiometric mixtures was carried out inside evacuated glass ampoules at temperatures close to, but just below, the melting point. These were annealed as pellets at the appropriate temperature, with several intermediate grindings, until no further change was observed or a single-phase sample was obtained. Samples containing CuI were often more readily prepared by evaporation to dryness of an acetonitrile solution in which the constituent iodides had been dissolved. Similarly, the KBr containing compound K_2CuBr_3 was prepared by precipitation from a hot aqueous solution of KBr and CuBr. Mixtures containing AgCl were first melted in an evacuated ampoule before the annealing procedure was performed. In several cases the final samples contained evidence of additional phases. These are listed in Table 1 and were present in sufficiently small amounts (less than a few %) that they can be assumed to have no significant effect on the diffraction or ionic conductivity measurements. The latter is supported by the absence of any notable effects within the temperature dependent conductivity data caused by phase transitions within, or melting of, the impurity phases. Nevertheless, some care should be taken when making detailed comparisons between the absolute values of the ionic conductivities of different samples.

Measurements of the ionic conductivities of the samples used the two-terminal method with impedance and admittance spectra collected over the frequency range 10^{-1}–10^7 Hz using a Solartron S1260 Frequency Response Analyser. Details of this device can be found elsewhere [23]. Pelleted samples of typical dimensions 5 mm diameter and 5 mm length were held between spring loaded platinum contacts and heated at rates between 0.5 and 1.0 K min^{-1}. Differences in the ionic conductivity were typically observed between the heating and cooling runs of the first heating/cooling cycle, due to pellet sintering effects and changes in the quality of the contacts to the sample. The results presented were all collected during a second heating run.

Diffraction data were collected using both neutron and X-ray techniques. The former has the disadvantage

Table 1
Summary of the preparation methods used to synthesize the various powder samples studied in the course of this work. The additional phases observed as minor impurities within the samples are listed

Compound	Sample preparation	Additional phases
Cs_2AgCl_3	Solid state reaction for 2 weeks at 473 K	$CsAgCl_2$
Rb_2AgBr_3	Solid state reaction for 2 weeks at 513 K	None
Cs_2AgBr_3	Solid state reaction for 2 weeks at 513 K	CsBr
K_2AgI_3	Solid state reaction for 8 weeks at 373 K	KI
Rb_2AgI_3	Solid state reaction for 2 weeks at 493 K	RbI
Cs_2AgI_3	Solid state reaction for 2 weeks at 493 K	$CsAg_2I_3$ and CsI
K_2CuCl_3	Solid state reaction for 4 weeks at 398 K	KCl
K_2CuBr_3	Precipitated from a hot aqueous solution	KBr
Rb_2CuCl_3	Solid state reaction for 30 h at 473 K	RbCl
Rb_2CuBr_3	Solid state reaction for 2 weeks at 513 K	RbBr
$Cs_3Cu_2Cl_5$	Solid state reaction for 5 days at 543 K	CsCl
$Cs_3Cu_2Br_5$	Solid state reaction for 5 days at 543 K	None
$Cs_3Cu_2I_5$	Precipitated from acetonitrile solution	None
$CsAgCl_2$	Solid state reaction for 2 weeks at 538 K	CsCl and AgCl
$CsAgBr_2$	Solid state reaction for 2 weeks at 503 K	CsBr and AgBr
$CsCu_2Cl_3$	Solid state reaction for 60 h at 533 K	None
$CsCu_2Br_3$	Solid state reaction for 60 h at 583 K	None
$CsCu_2I_3$	Precipitated from acetonitrile solution	None
$RbCu_2Br_3$	Solid state reaction for 60 h at 533 K	None
$RbCu_2I_3$	Precipitated from acetonitrile solution	None
$CsAg_2I_3$	Solid state reaction for 60 h at 483 K	None

of requiring larger samples, but allows easier access to high temperature studies. In addition, the absence of a form-factor for neutron scattering provides the diffraction data to shorter *d*-spacings which are essential to probe thermal motion and disorder. For these reasons, neutron diffraction was preferred for the study of those compounds exhibiting high temperature phase transitions or highly anisotropic thermal vibrations. The majority of the powder neutron diffraction experiments were performed on the Polaris diffractometer at the ISIS facility, UK [24] with around 5 g of sample contained inside thin walled vanadium cans of ~11 mm diameter. X-ray diffraction data were collected using a STOE STADI-P diffractometer ($CuK\alpha_1$ radiation) over the 2θ range 8–88° using a position sensitive detector that was moved in steps of 0.2°. X-ray data for the Rb_2AgI_3, Cs_2AgI_3 and $Cs_3Cu_2Cl_5$ compounds was collected at the beam line BM16 at the ESRF, Grenoble, over the 2θ range 1–18° with $\lambda = 0.310272$ Å. Indexing and Rietveld refinement of the powder diffraction data used the programs TREOR [25] and GSAS [26], respectively. The quality of the fits was assessed using the usual goodness-of-fit *R*-factors, R_{WP} and R_P [27].

3. Results

In the following subsections we consider each stoichiometry in turn, summarizing the known compounds and the state of knowledge concerning their crystal structures, followed by the results of our least-squares refinements. Further discussion of their respective ionic arrangements will be given in Section 4.3 using representative examples of each structure type.

3.1. M_2AX_3 compounds

Of the possible 18 compounds of stoichiometry M_2AX_3 (M = K, Rb, Cs; A = Cu, Ag and X = Cl, Br, I) a total of 12 have been identified on the basis of DTA/DSC studies of their binary phase diagrams and/or X-ray diffraction investigations. These are Rb_2AgCl_3 [28], Cs_2AgCl_3 [29], Rb_2AgBr_3 [17], Cs_2AgBr_3 [17], K_2AgI_3 [16,17,30,31], Rb_2AgI_3 [17,30,32], Cs_2AgI_3 [17], K_2CuCl_3 [21,29,33], Rb_2CuCl_3 [34], K_2CuBr_3 [35], Rb_2CuBr_3 [21] and Rb_2CuI_3 [17]. Of these, only Rb_2AgCl_3 [28], K_2AgI_3 [31] and Rb_2AgI_3 [32] have been the subject of full structural characterization, in which positional parameters have been determined by least-squares methods. However, the unit cell dimensions of a number of the other compounds have been reported [29,30] and it is generally accepted that all adopt one of three closely related structure types, which we label I, II and III. Structure type III is adopted by $(NH_4)_2CuCl_3$ [36] and, whilst it might be considered a likely structure for large M^+ such as Cs^+, it is not observed in any of the compounds studied here and is not discussed further.

X-ray diffraction studies of 10 compounds of stoichiometry M_2AX_3 have been performed in the course of this work. Those omitted from the list of 12 given at the start of this section are Rb_2AgCl_3, because it has been the subject of a very recent single-crystal study [28], and Rb_2CuI_3. In the latter case, large amounts of unreacted RbI were always found when attempting to prepare this composition, together with the hydrated compound $Rb_2Cu_2I_4 \cdot H_2O$ [37]. It should also be noted that K_2CuI_3 and Cs_2CuI_3 do not exist either. The remaining 4 compounds of the 18 possible should be K_2AgCl_3, K_2AgBr_3, Cs_2CuCl_3 and Cs_2CuBr_3. However, the KX–AgX (X=Cl and Br) systems are simple eutectics [17], whilst the CsX–CuX (X=Cl and Br) systems contain phases of stoichiometry $Cs_3Cu_2X_5$ instead (see Section 3.2). All the compounds studied in this work were found to exist in one of the two structure types labelled I and II. Indexing of the X-ray diffraction data provided unit cells of dimensions consistent with the known sizes of either the type-I or type-II compounds, after allowing for the relative sizes of the constituent ions. Rietveld refinements of the data using the appropriate structural model gave good fits in all cases, with the R-factors listed in Table 2. The suggestion that K_2CuCl_3 possesses $Pna2_1$ rather than $Pnma$ symmetry [33] is not supported by this work. Two typical examples of the quality of the fits to the experimental data are illustrated for the cases Rb_2AgI_3 (structure type I) and Cs_2AgI_3 (structure type II) in Fig. 1.

Structure types I and II are closely related and the first co-ordination shell around both the A^+ and M^+ cations is almost identical in both cases. The A^+ species lie at the center of tetrahedra of anions whilst the two symmetry independent M^+ sites lie at the center of rather irregular 7-fold polyhedra. As illustrated in Fig. 2, the AX_4 tetrahedra form infinite corner-sharing strings (parallel to [010] in both cases). However, the arrangement of these strings is different in the two structure types, with the symmetry independent $M1$ and $M2$ sites in structure type I surrounded by 2 and 4 tetrahedral strings, respectively, whilst both are surrounded by three strings in structure type II.

It has been proposed that the type II structure is preferentially formed if r_X/r_M is small [38]. However, this suggestion is not supported by the structural assignments presented in Table 2 and, instead, it appears that structure type II is favored if r_A/r_M is small. The measured ionic conductivities of the M_2AgX_3 and M_2CuX_3 phases are illustrated in Figs. 3 and 4, respectively. All the compounds are relatively poor conductors at temperatures close to ambient, with no evidence that either structure type is significantly more suited to diffusion of the A^+ ions. Indeed, there appears no systematic manner in which the relative conductivities of the M_2AX_3 compounds can be rationalized, though there is a slight trend towards higher conductivities in those compounds containing the smaller M^+ ions. This is somewhat counterintuitive, since these compounds have smaller unit cell volumes and might be expected to possess more restricted diffusion pathways. The ionic conductivities increase relatively rapidly with temperature, but the rather low melting/decomposition temperatures of the M_2AX_3 compounds precludes reaching values of σ generally considered characteristic of 'superionic' conduction. There is no evidence of any structural phase transitions within any of the compounds on heating.

3.2. $M_3A_2X_5$ compounds

The presence of the three compounds $Cs_3Cu_2Cl_5$, $Cs_3Cu_2Br_5$ and $Cs_3Cu_2I_5$ was established by DTA studies of the respective phase diagrams [21]. $Cs_3Cu_2I_5$ has been reported to adopt an orthorhombic structure in space group $Pbnm$ [39]. The M^+ are distributed over two symmetry independent sites, with irregular 8-fold co-ordination to the anions. There are also two types of Cu^+, one of which (Cu2) resides within a tetrahedrally co-ordinated interstice within the anion sublattice and the other (Cu1) occupies a trigonal site. By contrast, $Cs_3Cu_2Cl_5$ has been suggested to adopt a different orthorhombic structure in space group $Cmcm$, in which the Cu^+ are disordered over two sites which are tetrahedrally co-ordinated to Cl^- [40]. To the authors' knowledge, no structural study of $Cs_3Cu_2Br_5$ has been reported.

X-ray diffraction data for the three $Cs_3Cu_2X_3$ compounds showed that all three could be indexed on the basis of an orthorhombic unit cell, with reflection conditions consistent with space group $Pnma$ (the standard setting of $Pbnm$). As a result, the structural model reported for $Cs_3Cu_2I_5$ [39] was used as a starting model for the refinements in all three cases. The quality of the fits confirmed that all three compounds are isostructural, with the parameters listed in Table 3. It was also observed that $Cs_3Cu_2Cl_5$ decomposes in air to form the phase with disordered Cu^+ crystallizing in space group $Cmcm$ [40].

The representative structure of $Cs_3Cu_2I_5$ is shown in Fig. 5 and illustrates the 3- and 4-fold co-ordination of the two Cu^+ sites. The modest ionic conductivities of the three $Cs_3Cu_2X_3$ compounds are shown in Fig. 6, with σ for the $X = I^-$ material somewhat lower than the other two.

3.3. MAX_2 compounds

In the case of stoichiometry MAX_2, the only two compounds reported are $CsAgCl_2$ [41] and $CsAgBr_2$ [42].

Table 2
Summary of the structural properties of the compounds of stoichiometry M_2AX_3 determined by Rietveld refinement of powder X-ray diffraction data, except for Rb_2AgCl_3, for which the information is taken from a recent publication [28]

M_2AX_3	Rb_2AgCl_3	Cs_2AgCl_3	Rb_2AgBr_3	Cs_2AgBr_3	K_2AgI_3	Rb_2AgI_3	Cs_2AgI_3	K_2CuCl_3	K_2CuBr_3	Rb_2CuCl_3	Rb_2CuBr_3
Type	I	II	I	II	I	I	II	II	II	II	II
Sp. gr.	*Pnma* [28]	*Pnma*	*Pnma*	*Pnma*	*Pnma*	*Pnma*	*Pnma*	*Pnma*	*Pnma*	*Pnma*	*Pnma*
a (Å)	9.205(3)	13.2098(6)	9.5772(2)	13.7549(5)	10.0007(2)	10.2376(1)	14.5875(2)	12.0302(6)	12.6066(4)	12.5010(7)	13.0729(4)
b (Å)	4.482(1)	4.5514(2)	4.6458(1)	4.7192(2)	4.77201(9)	4.89791(5)	4.95097(7)	4.1483(2)	4.3361(1)	4.2721(3)	4.4515(1)
c (Å)	17.8738(1)	13.7580(7)	18.6629(4)	14.3623(5)	19.5105(4)	19.9838(2)	15.2983(2)	12.5869(7)	13.2470(5)	13.0000(9)	13.6414(4)
$M1^+$											
x	0.5786(2)	0.1716(3)	0.5772(3)	0.1721(3)	0.5779(9)	0.5768(4)	0.1758(2)	0.1721(6)	0.1746(5)	0.1719(4)	0.1727(3)
y	$\frac{1}{4}$	$\frac{1}{4}$	$\frac{1}{4}$	$\frac{1}{4}$	$\frac{1}{4}$	$\frac{1}{4}$	$\frac{1}{4}$	$\frac{1}{4}$	$\frac{1}{4}$	$\frac{1}{4}$	$\frac{1}{4}$
z	0.7872(1)	0.4819(4)	0.7881(2)	0.4806(3)	0.7866(5)	0.7897(2)	0.4808(2)	0.4814(6)	0.4824(6)	0.4766(5)	0.4750(3)
B_{iso} (Å^2)	2.04(3)	4.0(1)	3.3(1)	3.8(1)	3.9(3)	2.8(1)	3.0(1)	2.0(2)	3.8(2)	4.1(1)	4.3(1)
$M2^+$											
x	0.2391(2)	0.5118(4)	0.2443(4)	0.5125(3)	0.2449(9)	0.2513(4)	0.5144(2)	0.5114(6)	0.5132(5)	0.5126(4)	0.5123(3)
y	$\frac{1}{4}$	$\frac{1}{4}$	$\frac{1}{4}$	$\frac{1}{4}$	$\frac{1}{4}$	$\frac{1}{4}$	$\frac{1}{4}$	$\frac{1}{4}$	$\frac{1}{4}$	$\frac{1}{4}$	$\frac{1}{4}$
z	0.4562(1)	0.6738(4)	0.4573(2)	0.6738(3)	0.4586(5)	0.4571(2)	0.6763(2)	0.6767(7)	0.6794(8)	0.6728(4)	0.6761(3)
B_{iso} (Å^2)	2.09(3)	3.9(1)	3.6(1)	3.5(1)	4.2(3)	3.1(1)	3.4(1)	2.0(2)	4.9(2)	2.6(1)	3.4(1)
A^+											
x	0.1213(2)	0.2558(4)	0.1271(3)	0.2548(3)	0.1284(3)	0.1357(3)	0.2546(3)	0.2543(5)	0.2531(4)	0.2549(6)	0.2543(4)
y	$\frac{1}{4}$	$\frac{1}{4}$	$\frac{1}{4}$	$\frac{1}{4}$	$\frac{1}{4}$	$\frac{1}{4}$	$\frac{1}{4}$	$\frac{1}{4}$	$\frac{1}{4}$	$\frac{1}{4}$	$\frac{1}{4}$
z	0.1311(1)	0.1996(5)	0.1342(2)	0.1959(3)	0.1351(2)	0.1356(1)	0.1919(3)	0.1971(4)	0.1972(4)	0.1877(7)	0.1896(4)
B_{iso} (Å^2)	2.58(3)	4.8(1)	4.4(1)	3.8(2)	4.6(1)	3.9(1)	4.4(1)	4.1(2)	4.6(1)	4.3(1)	4.7(2)
$X1^-$											
x	0.1847(5)	0.137(1)	0.1862(3)	0.1385(5)	0.1887(3)	0.1888(2)	0.1332(2)	0.1386(8)	0.1331(3)	0.1419(9)	0.1381(3)
y	$\frac{1}{4}$	$\frac{1}{4}$	$\frac{1}{4}$	$\frac{1}{4}$	$\frac{1}{4}$	$\frac{1}{4}$	$\frac{1}{4}$	$\frac{1}{4}$	$\frac{1}{4}$	$\frac{1}{4}$	$\frac{1}{4}$
z	0.2729(2)	0044(1)	0.2756(2)	0.0469(4)	0.2770(2)	0.2757(1)	0.0487(2)	0.0516(7)	0.0524(3)	0.0555(9)	0.0517(3)
B_{iso} (Å^2)	2.05(8)	3.9(2)	3.6(1)	2.9(2)	3.5(1)	2.8(1)	3.2(1)	2.6(3)	2.8(1)	2.5(2)	2.8(1)
$X2^-$											
x	0.3784(5)	0.442(1)	0.3803(4)	0.4420(5)	0.3805(3)	0.3814(2)	0.4422(2)	0.4446(8)	0.4416(3)	0.4354(9)	0.4366(3)
y	$\frac{1}{4}$	$\frac{1}{4}$	$\frac{1}{4}$	$\frac{1}{4}$	$\frac{1}{4}$	$\frac{1}{4}$	$\frac{1}{4}$	$\frac{1}{4}$	$\frac{1}{4}$	$\frac{1}{4}$	$\frac{1}{4}$
z	0.0727(2)	0.134(1)	0.0715(2)	0.1392(5)	0.0708(2)	0.0708(1)	0.1368(2)	0.1407(7)	0.1377(3)	0.1397(9)	0.1384(3)
B_{iso} (Å^2)	2.13(8)	2.5(2)	3.1(1)	5.2(3)	3.4(1)	2.6(1)	3.6(1)	3.2(3)	3.2(1)	2.9(2)	4.0(1)
$X3^-$											
x	0.5066(5)	0.274(1)	0.5039(3)	0.2757(4)	0.5102(3)	0.4984(2)	0.2764(2)	0.2735(7)	0.2757(3)	0.2748(8)	0.2755(3)
y	$\frac{1}{4}$	$\frac{1}{4}$	$\frac{1}{4}$	$\frac{1}{4}$	$\frac{1}{4}$	$\frac{1}{4}$	$\frac{1}{4}$	$\frac{1}{4}$	$\frac{1}{4}$	$\frac{1}{4}$	$\frac{1}{4}$
z	0.5974(2)	0.791(2)	0.5986(2)	0.7897(4)	0.5983(1)	0.6006(1)	0.7857(2)	0.7911(6)	0.7946(3)	0.7798(9)	0.7825(2)
B_{iso} (Å^2)	2.10(8)	7.0(2)	3.6(1)	2.9(2)	3.8(1)	2.7(1)	2.9(1)	2.2(3)	2.7(1)	3.1(2)	2.8(1)
R_{WP} (%)	9.4	4.08	3.94	2.60	3.86	7.91	6.60	2.85	5.03	4.53	3.15
R_P (%)	—	3.10	2.89	1.98	2.83	6.34	5.32	2.12	3.77	3.34	2.32
χ^2	—	0.44	0.92	0.52	1.02	1.52	1.36	0.41	0.54	0.45	0.71
N_D	—	3949	3949	3949	3949	4212	3999	3949	3949	3949	3949
N_V	43	60	29	36	33	55	53	35	51	52	37
N_P	741	488	373	430	428	639	1101	300	337	325	367

B_{iso} is the refined isotropic thermal vibration parameter. The weighted profile (WP) and profile (P) R-factors are given by

$$R_{WP}^2 = \sum_{N_D} \frac{(I_{obs} - I_{calc})^2}{(\sigma I_{obs})^2} \Big/ \sum_{N_D} \frac{(I_{obs})^2}{(\sigma I_{obs})^2} \quad \text{and} \quad R_P^2 = \sum_{N_D} (I_{obs} - I_{calc})^2 \Big/ \sum_{N_D} (I_{obs})^2,$$

respectively, and the goodness-of-fit parameter χ^2 is given by

$$\chi^2 = \sum_{N_D} \frac{(I_{obs} - I_{calc})^2}{(\sigma I_{obs})^2} / (N_D - N_V).$$

The summations are made over the N_D data points used in the fit. I_{obs} and I_{calc} are the observed and calculated intensities, respectively, and σI_{obs} is the estimated standard deviation on I_{obs} derived from the counting statistics. N_V is the number of fitted variables and N_P is the number of Bragg peaks within the fitted data range. The values within parentheses represent the estimated standard deviations on the fitted parameters.

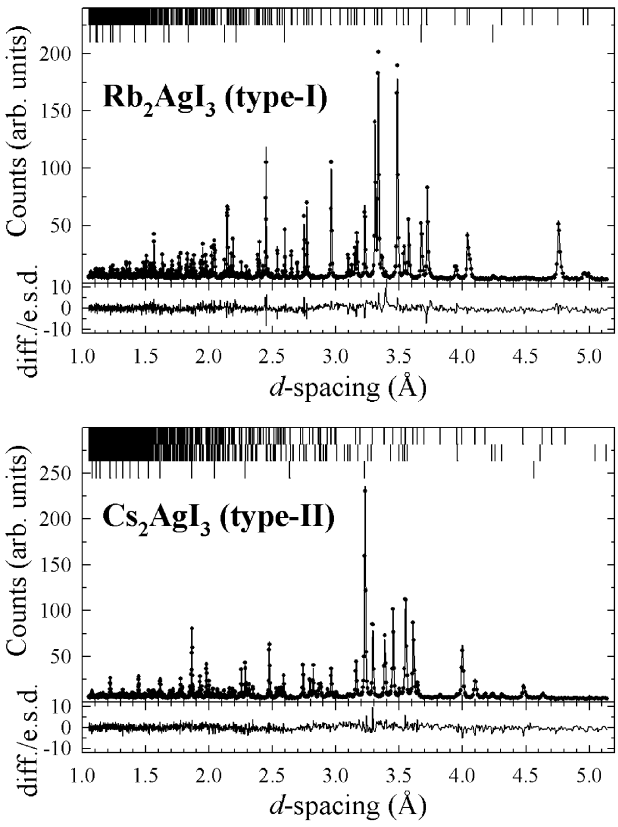

Fig. 1. The least-squares fits to the powder X-ray diffraction data collected from Rb_2AgI_3 (structure type-I, top) and Cs_2AgI_3 (structure type-II, bottom) at ambient temperature. The dots are the experimental data points (with fitted background subtracted) and the solid line is the calculated profile using the parameters listed in Table 2. The lower trace shows the difference (measured minus calculated) divided by the estimated standard deviation on the experimental data points. The rows of tick marks along the top of the figures denote the calculated positions of all the symmetry allowed Bragg reflections. In the upper figure these are Rb_2AgI_3 (top) and RbI (bottom), whilst in the lower figure they are Cs_2AgI_3 (top), $CsAg_2I_3$ (middle) and CsI (bottom).

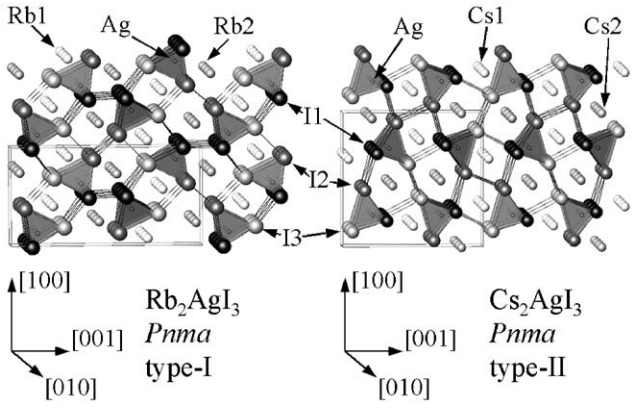

Fig. 2. Comparison of the crystal structures of Rb_2AgI_3 (structure type-I, left) and Cs_2AgI_3 (structure type-II, right) showing the two different arrangements of the one-dimensional strings of corner-sharing AgI_4 tetrahedra.

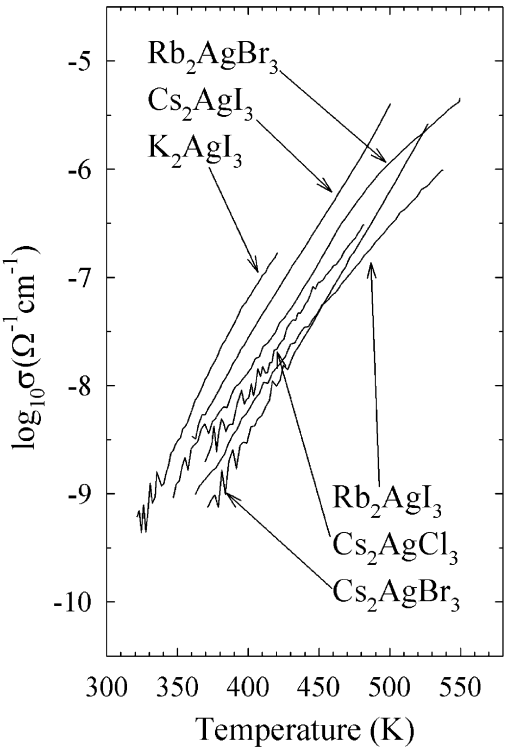

Fig. 3. The temperature variation of the ionic conductivity $\log_{10}\sigma$ of the six compounds of stoichiometry M_2AgX_3. The apparent jitter in the data within the lower temperature region is due to the resistance of the sample approaching the upper limit of the measurement apparatus.

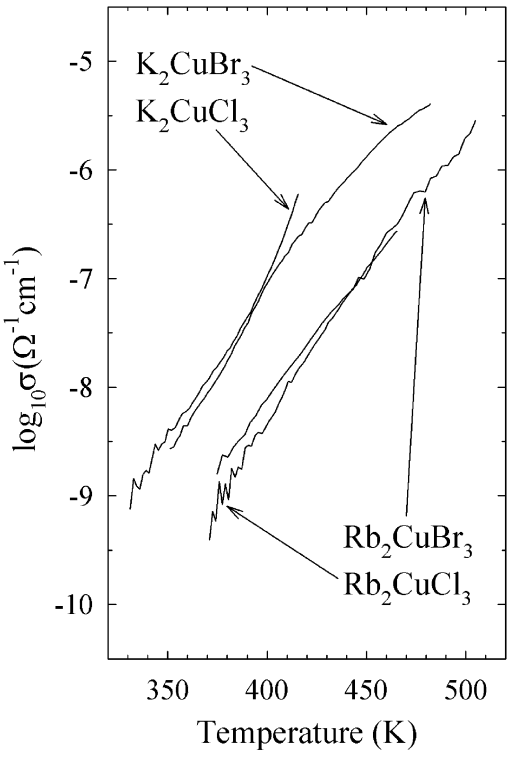

Fig. 4. The temperature variation of the ionic conductivity $\log_{10}\sigma$ of the four compounds of stoichiometry M_2CuX_3. The apparent jitter in the data within the lower temperature region is due to the resistance of the sample approaching the upper limit of the measurement apparatus.

Table 3
Summary of the structural properties of the compounds of stoichiometry $M_3A_2X_3$ determined by Rietveld refinement of powder X-ray diffraction data (X = Br and I) and neutron diffraction data (X = Cl). The latter were collected at the Swedish research reactor at the NFL, Studsvik, using a wavelength of 1.47 Å and with the sample placed in a thin-walled vanadium can.

$M_3A_2X_5$ Space group	$Cs_3Cu_2Cl_5$ *Pnma*	$Cs_3Cu_2Br_5$ *Pnma*	$Cs_3Cu_2I_5$ *Pnma*
a (Å)	9.176(4)	9.5240(9)	10.1743(1)
b (Å)	10.505(4)	10.979(1)	11.6532(2)
c (Å)	13.141(6)	13.648(1)	14.3621(2)
$M1^+$			
x	0.602(5)	0.597(1)	0.5948(5)
y	$\frac{1}{4}$	$\frac{1}{4}$	$\frac{1}{4}$
z	0.563(5)	0.5459(7)	0.5506(4)
B_{iso} (Å^2)	1.5(7)	3.3(3)	2.5(1)
$M2^+$			
x	0.047(3)	0.0529(7)	0.0524(4)
y	0.988(4)	0.9964(8)	0.9897(4)
z	0.685(3)	0.6784(4)	0.6783(2)
B_{iso} (Å^2)	$=B_{M1}$	4.9(2)	3.9(1)
$A1^+$			
x	0.278(6)	0.251(3)	0.2409(11)
y	$\frac{1}{4}$	$\frac{1}{4}$	$\frac{1}{4}$
z	0.365(5)	0.368(2)	0.3701(8)
B_{iso} (Å^2)	9(1)	13(1)	6.9(4)
$A2^+$			
x	0.235(6)	0.204(2)	0.2125(9)
y	$\frac{1}{4}$	$\frac{1}{4}$	$\frac{1}{4}$
z	0.531(5)	0.550(2)	0.5473(7)
B_{iso} (Å^2)	$=B_{A1}$	10.7(8)	3.6(3)
$X1^-$			
x	0.692(3)	0.682(1)	0.6918(3)
y	0.562(2)	0.5601(8)	0.5609(3)
z	0.557(2)	0.5560(9)	0.5516(3)
B_{iso} (Å^2)	3.1(4)	4.2(3)	2.5(1)
$X2^-$			
x	0.171(4)	0.165(2)	0.1574(5)
y	$\frac{1}{4}$	$\frac{1}{4}$	$\frac{1}{4}$
z	0.200(3)	0.209(1)	0.2069(4)
B_{iso} (Å^2)	$=B_{X1}$	6.3(6)	3.9(2)
$X3^-$			
x	0.988(4)	0.961(2)	0.9682(5)
y	$\frac{1}{4}$	$\frac{1}{4}$	$\frac{1}{4}$
z	0.507(3)	0.510(1)	0.5108(4)
B_{iso} (Å^2)	$=B_{X1}$	2.6(5)	2.7(2)
$X4^-$			
x	0.300(4)	0.301(2)	0.3012(6)
y	$\frac{1}{4}$	$\frac{1}{4}$	$\frac{1}{4}$
z	0.715(3)	0.718(1)	0.7163(4)
B_{iso} (Å^2)	$=B_{X1}$	4.3(6)	3.1(2)
R_{WP}(%)	9.72	4.63	8.71
R_P(%)	7.71	3.42	7.09
χ^2	1.56	0.56	1.35
N_D	1132	3949	3997
N_V	38	37	53
N_P	761	581	1083

B_{iso} is the refined isotropic thermal vibration parameter. The weighted profile (WP) and profile (P) R-factors are given by

$$R_{WP}^2 = \sum_{N_D} \frac{(I_{obs} - I_{calc})^2}{(\sigma I_{obs})^2} / \sum_{N_D} \frac{(I_{obs})^2}{(\sigma I_{obs})^2}$$

and

$$R_P^2 = \sum_{N_D} (I_{obs} - I_{calc})^2 / \sum_{N_D} (I_{obs})^2,$$

respectively, and the goodness-of-fit parameter χ^2 is given by

$$\chi^2 = \sum_{N_D} \frac{(I_{obs} - I_{calc})^2}{(\sigma I_{obs})^2} / (N_D - N_V).$$

The summations are made over the N_D data points used in the fit. I_{obs} and I_{calc} are the observed and calculated intensities, respectively, and σI_{obs} is the estimated standard deviation on I_{obs} derived from the counting statistics. N_V is the number of fitted variables and N_P is the number of Bragg peaks within the fitted data range. The values within parentheses represent the estimated standard deviations on the fitted parameters.

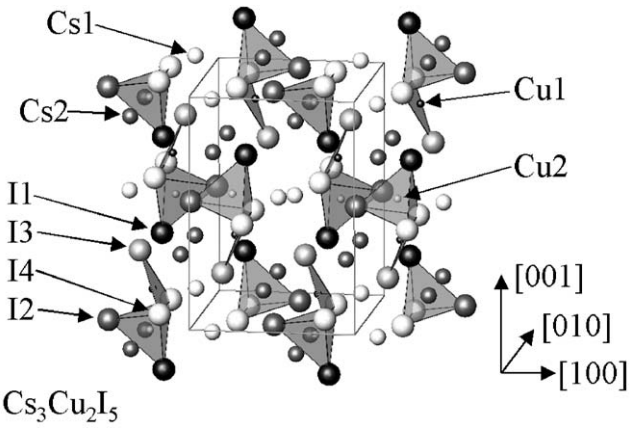

Fig. 5. The crystal structure of $Cs_3Cu_2I_5$ showing the Cu^+ positions with planar 3-fold (Cu1) and tetrahedral (Cu2) co-ordinations.

Under ambient conditions they are isostructural, with space group *Cmcm*. The major peaks observed in the neutron diffraction data for both $CsAgCl_2$ and $CsAgBr_2$ could be ascribed to the published unit cells of each phase, though a number of weak additional reflections were also observed and identified as a small fractions of unreacted AgCl (AgBr) and CsCl (CsBr). Three phase refinements of the diffraction data were performed and gave satisfactory fits, as illustrated for the case of $CsAgCl_2$ in Fig. 7. The refined parameters for $CsAgCl_2$ and $CsAgBr_2$ are listed in Table 4 and are very close to those published previously [41,42].

The temperature dependence of the ionic conductivities of the compounds $CsAgCl_2$ and $CsAgBr_2$ is shown in Fig. 8, with σ_i relatively low in both cases. Both

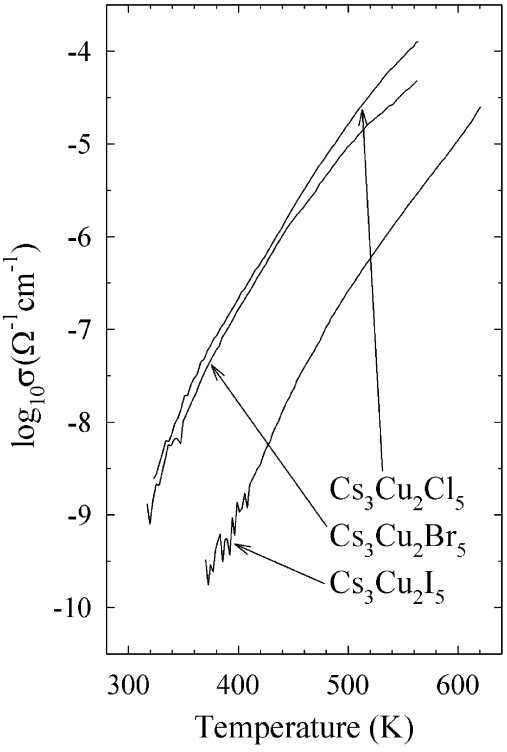

Fig. 6. The temperature variation of the ionic conductivity $\log_{10}\sigma$ of the three compounds of stoichiometry $M_3A_2X_5$. The apparent jitter in the data within the lower temperature region is due to the resistance of the sample approaching the upper limit of the measurement apparatus.

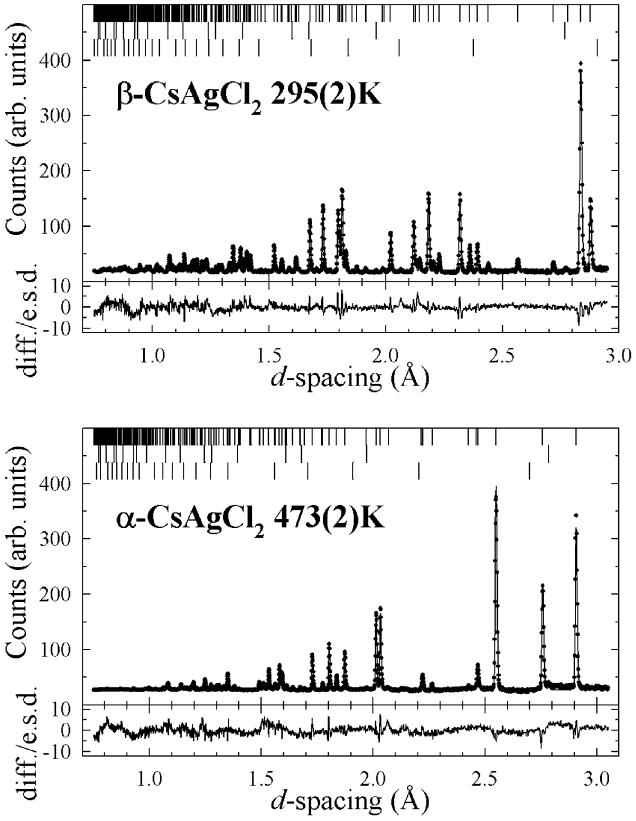

Fig. 7. The least-squares fit to the powder neutron diffraction data collected from the β phase at 295(2) K (top) and the α phase at 473(2) K (bottom) of $CsAgCl_2$. The dots are the experimental data points (with fitted background subtracted) and the solid line is the calculated profile using the parameters listed in Table 4. The lower trace shows the difference (measured minus calculated) divided by the estimated standard deviation on the experimental data points. The three rows of tick marks along the top of the figure denote the calculated positions of all the symmetry allowed Bragg reflections for $CsAgCl_2$ (top), CsCl (middle) and AgCl (bottom).

compounds are reported to undergo structural phase transitions on heating, at 443 K ($CsAgCl_2$) and 408 K ($CsAgBr_2$) [41,42]. There is no evidence of either transition in the ionic conductivity data, except for a possible slight change in the slope of $\log_{10}\sigma$ versus T for $CsAgCl_2$ at $\approx$425 K. Neutron diffraction data collected on heating $CsAgCl_2$ and $CsAgBr_2$ showed abrupt changes in the diffraction pattern indicative of a structural phase transition in each material at 408(5) and 413(8) K, respectively. In both cases there is considerable hysteresis, with the diffraction pattern reverting to that characteristic of the ambient temperature phase at 315(8) and 310(10) K, respectively. We denote the low and high temperature phases by β and α, respectively.

The structure of α-$CsAgCl_2$ was determined using neutron diffraction data collected at 473(2) K. The diffraction peaks could be successfully indexed using a tetragonal unit cell of dimensions $a\approx5.11$ Å and $c\approx9.86$ Å. The reflection conditions, $h+k=2n$ for $hk0$ reflections and $k=2n$ for $0k0$ reflections are consistent with space groups $P4/n$ and $P4/nmm$. A search of the ICSD crystallographic database [43] suggested that $CsLiCl_2$ provides a plausible structural model, since it is described by a unit cell of dimensions $a=4.924$ Å and $c=9.500$ Å and possesses space group $P4/nmm$ [44]. Calculations of the neutron diffraction profile using the unit cell for α-$CsAgCl_2$ and ionic positions based on those published for $CsLiCl_2$ [44] showed a good agreement with the measured data. The validity of this structural model was confirmed by Rietveld refinements of the data, which gave $R_{WP}=0.90\%$. The final fit is illustrated in Fig. 7 and details of the final refinement are given in Table 4. A similar procedure for the case of α-$CsAgBr_2$ also provided a tetragonal unit cell ($a\approx5.32$ Å and $c\approx10.21$ Å) and confirmed that the phase is isostructural with $CsLiCl_2$ (and, therefore, with $CsAgCl_2$). Its structural parameters are also detailed in Table 4.

The relationship between the β and α phases of the two $CsAgX_2$ compounds is illustrated for the case of X =Br in Fig. 9. The volume changes on heating are $\approx$5.6% in $CsAgCl_2$ and $\approx$5.3% in $CsAgBr_2$. In the β

phase the Ag^+ reside at the center of a distorted trigonal bipyramid of anions which becomes a more regular square pyramidal arrangement above the $\beta \rightarrow \alpha$ phase transition. In addition, alternate layers of the edge-sharing AgX_5 units are shifted by $c/2$ along [001], such that the relative orientation of neighboring layers becomes the same in both [001] and [100] directions (which are the [100] and [010] directions in the α-$CsAgX_2$ phases). This causes the anion co-ordination around the Cs^+ to increase from 8 to 9. The relative similarity of the structures of the β and α phases of the two $CsAgX_2$ phases probably explains the absence of any noticeable signature of the $\beta \rightarrow \alpha$ transition within the ionic conductivity data (Fig. 8).

Table 4
Summary of the structural properties of the two phases of the two compounds of stoichiometry MAX_2 determined by Rietveld refinement of powder neutron diffraction data

Phase	β		α	
MAX_2	$CsAgCl_2$	$CsAgBr_2$	$CsAgCl_2$	$CsAgBr_2$
T (K)	295(2)	295(2)	473(2)	423(2)
Space group	*Cmcm*	*Cmcm*	*P4/nmm*	*P4/nmm*
a (Å)	4.37637(2)	4.57430(3)	5.10938(2)	5.32370(3)
b (Å)	19.1863(1)	19.8944(2)	$=a$	$=a$
c (Å)	5.68515(2)	5.94714(4)	9.85955(7)	10.21183(8)
M^+				
x	0	0	$\frac{1}{4}$	$\frac{1}{4}$
y	0.5822(1)	0.5839(1)	$\frac{1}{4}$	$\frac{1}{4}$
z	$\frac{1}{4}$	$\frac{1}{4}$	0.7014(3)	0.7073(3)
B_{11} (Å^2)	1.52(9)	1.82(8)	5.2(1)	5.6(1)
B_{22} (Å^2)	1.96(9)	2.05(9)	$=B_{11}$	$=B_{11}$
B_{33} (Å^2)	2.65(9)	3.11(8)	3.5(1)	3.7(2)
A^+				
x	0	0	$\frac{1}{4}$	$\frac{1}{4}$
y	0.7995(1)	0.7995(1)	$\frac{1}{4}$	$\frac{1}{4}$
z	$\frac{1}{4}$	$\frac{1}{4}$	0.0986(3)	0.0996(3)
B_{11} (Å^2)	3.37(9)	3.21(6)	6.6(1)	6.3(1)
B_{22} (Å^2)	1.71(8)	1.71(7)	$=B_{11}$	$=B_{11}$
B_{33} (Å^2)	3.05(9)	3.55(8)	3.6(2)	3.3(1)
$X1^-$				
x	0	0	$\frac{1}{4}$	$\frac{1}{4}$
y	0.2239(1)	0.2251(1)	$\frac{3}{4}$	$\frac{3}{4}$
z	$\frac{1}{4}$	$\frac{1}{4}$	0	0
B_{11} (Å^2)	1.75(6)	1.77(7)	4.28(6)	4.40(8)
B_{22} (Å^2)	2.54(7)	2.83(7)	$=B_{11}$	$=B_{11}$
B_{33} (Å^2)	2.24(8)	1.59(7)	7.3(2)	6.4(2)
$X2^-$				
x	0	0	$\frac{1}{4}$	$\frac{1}{4}$
y	0.9310(1)	0.9311(1)	$\frac{1}{4}$	$\frac{1}{4}$
z	$\frac{1}{4}$	$\frac{1}{4}$	0.3534(2)	0.3566(3)
B_{11} (Å^2)	2.92(6)	2.61(6)	7.3(1)	7.4(1)
B_{22} (Å^2)	1.70(6)	1.53(5)	$=B_{11}$	$=B_{11}$
B_{33} (Å^2)	2.01(6)	2.39(6)	2.68(8)	2.6(1)

Table 4 (*continued*)

Phase	β		α	
R_{WP} (%)	1.56	1.65	0.90	1.01
R_P (%)	2.73	2.74	1.52	1.61
χ^2	3.76	5.13	2.58	4.15
N_D	2887	2864	2642	2698
N_V	39	44	19	39
N_P	564	637	339	376

B_{ij} are the components of the anisotropic thermal vibrations (defined by $B_{ij} = 8\pi^2 \langle u_{ij}^2 \rangle$, where u_{ij} is the mean-square amplitude of the vibration in direction ij). The weighted profile (WP) and profile (P) R-factors are given by

$$R_{WP}^2 = \sum_{N_D} \frac{(I_{obs} - I_{calc})^2}{(\sigma I_{obs})^2} / \sum_{N_D} \frac{(I_{obs})^2}{(\sigma I_{obs})^2}$$

and

$$R_P^2 = \sum_{N_D} (I_{obs} - I_{calc})^2 / \sum_{N_D} (I_{obs})^2,$$

respectively, and the goodness-of-fit parameter χ^2 is given by

$$\chi^2 = \sum_{N_D} \frac{(I_{obs} - I_{calc})^2}{(\sigma I_{obs})^2} / (N_D - N_V).$$

The summations are made over the N_D data points used in the fit. I_{obs} and I_{calc} are the observed and calculated intensities, respectively, and σI_{obs} is the estimated standard deviation on I_{obs} derived from the counting statistics. N_V is the number of fitted variables and N_P is the number of Bragg peaks within the fitted data range. The values within parentheses represent the estimated standard deviations on the fitted parameters.

3.4. MA_2X_3 compounds

The binary phase diagrams indicate the presence of six compounds of stoichiometry MA_2X_3, these being $CsAg_2I_3$ [17,45,46], $CsCu_2Cl_3$ [21,45,47], $CsCu_2Br_3$ [21,47], $RbCu_2Br_3$ [21], $RbCu_2I_3$ [17,39] and $CsCu_2I_3$ [21,48]. Of these, crystallographic studies of $CsCu_2Cl_3$ [47], $CsCu_2Br_3$ [47], $CsCu_2I_3$ [48] and $RbCu_2I_3$ [39] have been reported. These are based on X-ray diffraction studies and indicate that all four compounds are isostructural, with orthorhombic space group *Cmcm*.

Neutron powder diffraction data were collected for all six compounds of stoichiometry MA_2X_3 listed above. In all six cases, the data could be successfully indexed using orthorhombic unit cells of similar dimensions to those published previously [39,47,48]. Least-squares refinements of the neutron data were performed using the *Cmcm* structural model and, in all cases, a relatively good fit to the data was obtained. However, extremely large and anisotropic thermal vibrations of the $X2$ anions and the M cations were found, especially for the compounds $RbCu_2I_3$ and $CsAg_2I_3$. On closer inspection, the diffraction patterns of these two compounds show a number of relatively weak reflections which are consistent with the orthorhombic unit cells but whose $h\,k\,l$ indices violate the $h + k = 2n$ condition imposed by the

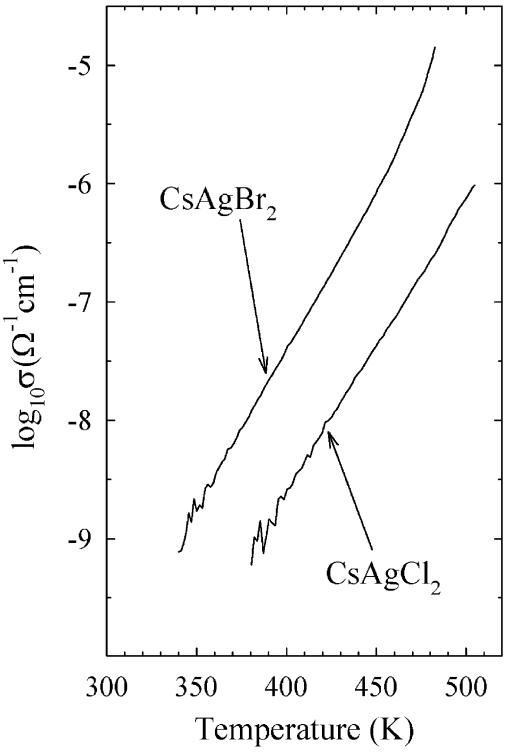

Fig. 8. The temperature variation of the ionic conductivity $\log_{10}\sigma$ of the two compounds of stoichiometry MAX_2. The apparent jitter in the data within the lower temperature region is due to the resistance of the sample approaching the upper limit of the measurement apparatus.

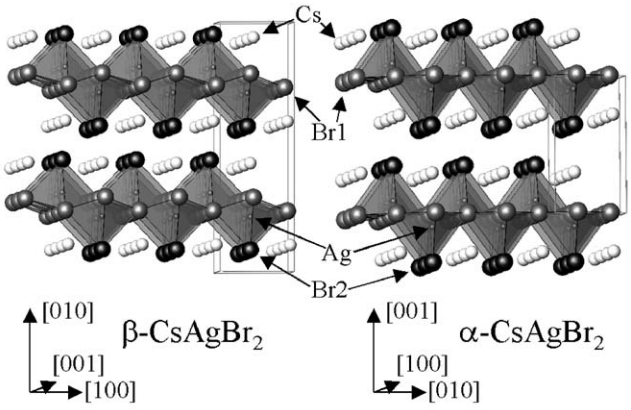

Fig. 9. Comparison of the crystal structures of the β (left) and α (right) phases of $CsAgBr_2$, showing the layers of edge-sharing $AgBr_5$ units and the more regular co-ordination polyhedra surrounding the Ag^+ in the latter case.

C-centering symmetry operation. This is illustrated for the case of $RbCu_2I_3$ in Fig. 10. A plausible explanation for this behavior has been proposed [45], in which the edge-sharing AX_4 tetrahedra are rotated about the c-axis, such that the symmetry is lowered from *Cmcm* to *Pbnm*. The latter is a non-standard setting of space group *Pnma* but is adopted here to illustrate the close

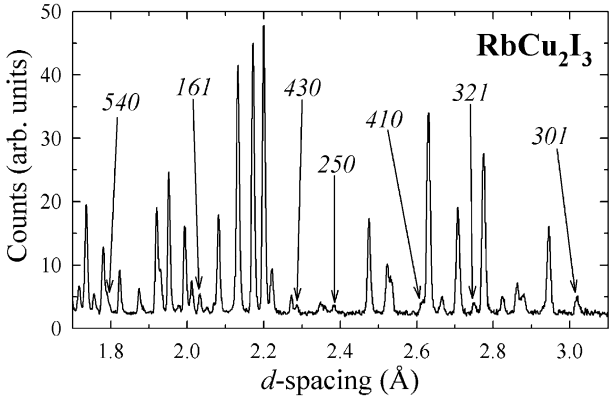

Fig. 10. Powder neutron diffraction data collected from $RbCu_2I_3$ at ambient temperature showing the presence of numerous hkl reflections with $h+k=2n+1$ which violate the absence conditions imposed by *Cmcm* symmetry.

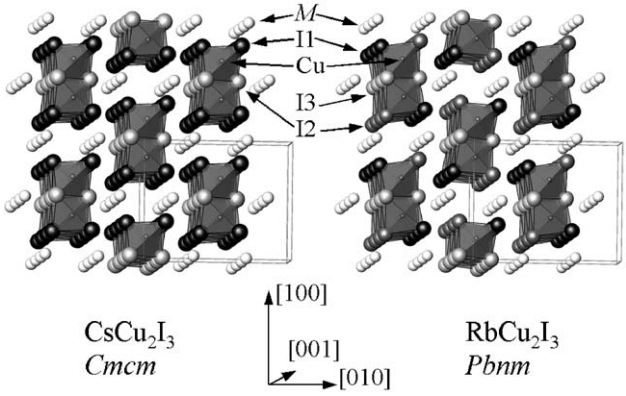

Fig. 11. Comparison of the crystal structures of $CsCu_2I_3$ (space group *Cmcm*, left) and $RbCu_2I_3$ (space group *Pbnm*, right) showing the slight rotation of the strings of CuI_4 tetrahedra about the [001] directions.

relationship between their structures. This process is illustrated in Fig. 11 and introduces six more variable positional parameters into the fitting procedure. Refinements using both models were compared for all six compounds. Significant reductions in R_{WP} were only observed in the case of $RbCu_2I_3$ and $CsAg_2I_3$. The final structural parameters are listed in Table 5. The *Pbnm* structure is equivalent to the *Cmcm* one if six conditions are met ($x_M=0$, $y_{Ag/Cu}=z_{Ag/Cu}=0, x_{X1}=0, x_{X2}=x_{X3}+1/2$ and $y_{X2}=y_{X3}+1/2$) and, with reference to Table 5, it is clear that the deviation from *Cmcm* symmetry is relatively small. Presumably, this explains why the distortion from the higher symmetry case was not reported previously [39]. The rotation of the tetrahedral chains within the *Pbnm* structure is $\theta \approx \tan^{-1}(-1/2+y_{X2}-y_{X3})/(3/2-x_{X2}-x_{X3})$, which is $\approx 1.24^\circ$ for $RbCu_2I_3$ and $\approx 0.65^\circ$ for $CsAg_2I_3$. It is, however, interesting to note that the four other compounds with this stoichiometry exhibit relatively

Table 5
Summary of the structural properties of the compounds of stoichiometry MA_2X_3 determined by Rietveld refinement of powder neutron diffraction data

MA_2X_3 Sp. Gr.	$CsCu_2Cl_3$ *Cmcm*	$CsCu_2Br_3$ *Cmcm*	$CsCu_2I_3$ *Cmcm*	$RbCu_2Br_3$ *Cmcm*	$RbCu_2I_3$ *Pbnm*	$CsAg_2I_3$ *Pbnm*
a (Å)	9.49808(8)	9.87123(7)	10.5479(1)	9.8563(1)	10.68235(9)	11.0763(2)
b (Å)	11.8868(1)	12.3478(1)	13.1725(1)	12.4120(2)	13.3463(1)	13.7432(2)
c (Å)	5.59440(4)	5.81321(3)	6.09718(5)	5.55222(5)	5.73732(4)	6.23064(6)
M^+						
x	0	0	0	0	−0.0155(3)	−0.0168(7)
y	0.6846(3)	0.6780(2)	0.6722(2)	0.6865(3)	0.6832(2)	0.6837(3)
z	$\frac{1}{4}$	$\frac{1}{4}$	$\frac{1}{4}$	$\frac{1}{4}$	$\frac{1}{4}$	$\frac{1}{4}$
B_{11} (Å^2)	3.2(1)	3.1(1)	4.1(1)	3.9(2)	$B_{iso}=4.31(6)$Å^2	$B_{iso}=4.6(1)$Å^2
B_{22} (Å^2)	3.7(1)	4.2(1)	5.1(1)	4.7(2)	—	—
B_{33} (Å^2)	2.1(1)	2.1(1)	1.30(9)	2.2(1)	—	—
A^+						
x	0.8358(2)	0.8440(2)	0.8510(1)	0.8355(2)	0.8402(1)	0.8366(2)
y	0	0	0	0	0.0059(1)	0.0028(5)
z	0	0	0	0	0.0021(4)	0.0077(8)
B_{11} (Å^2)	4.64(9)	3.58(6)	3.58(7)	3.4(1)	$B_{iso}=3.17(3)$Å^2	$B_{iso}=4.12(7)$ Å^2
B_{22} (Å^2)	6.2(1)	3.94(7)	3.67(6)	4.1(1)	—	—
B_{33} (Å^2)	3.77(7)	3.00(5)	3.62(5)	2.84(8)	—	—
B_{23}(Å^2)	2.22(8)	0.89(7)	0.55(7)	1.1(1)	—	—
$X1^-$						
x	0	0	0	0	0.0087(3)	0.0003(6)
y	0.1133(2)	0.1181(2)	0.1204(2)	0.1158(3)	0.1149(2)	0.1235(2)
z	$\frac{1}{4}$	$\frac{1}{4}$	$\frac{1}{4}$	$\frac{1}{4}$	$\frac{1}{4}$	$\frac{1}{4}$
B_{11} (Å^2)	2.92(8)	2.23(9)	2.2(1)	2.7(1)	$B_{iso}=1.75(5)$Å^2	$B_{iso}=2.54(8)$Å^2
B_{22} (Å^2)	2.73(8)	1.46(9)	1.3(1)	1.3(1)	—	—
B_{33} (Å^2)	1.67(7)	1.63(9)	2.0(1)	2.4(1)	—	—
$X2^-$						
x	0.7151(1)	0.7146(1)	0.7170(1)	0.7097(2)	0.6915(2)	0.6973(7)
y	0.8841(1)	0.8814(2)	0.8810(2)	0.8753(2)	0.8965(2)	0.8794(5)
z	$\frac{1}{4}$	$\frac{1}{4}$	$\frac{1}{4}$	$\frac{1}{4}$	$\frac{1}{4}$	$\frac{1}{4}$
B_{11} (Å^2)	3.12(6)	2.60(7)	2.97(9)	3.5(1)	$B_{iso}=2.56(7)$Å^2	$B_{iso}=3.5(1)$Å^2
B_{22} (Å^2)	4.31(7)	4.11(9)	4.0(1)	5.1(2)	—	—
B_{33} (Å^2)	1.95(6)	1.74(7)	1.68(9)	1.5(1)	—	—
B_{12}(Å^2)	−1.54(6)	−1.36(7)	−1.79(8)	−2.6(1)	—	—
$X3^-$						
x	0.2151(1)†	0.2146(1)†	0.2170(1)†	0.2097(2)†	0.2297(2)	0.2125(6)
y	0.3841(1)†	0.3814(2)†	0.3810(2)†	0.3753(2)†	0.3582(2)	0.3602(5)
z	$\frac{1}{4}$	$\frac{1}{4}$	$\frac{1}{4}$	$\frac{1}{4}$	$\frac{1}{4}$	$\frac{1}{4}$
B_{ij} (Å^2)	†	†	†	†	$B_{iso}=2.11(6)$Å^2	$B_{iso}=3.3(1)$Å^2
R_{WP}(%)	1.17	1.67	1.50	2.08	1.13	1.16
R_P(%)	1.94	2.45	2.48	3.35	1.81	2.01
χ^2	2.33	3.54	1.48	2.63	1.43	1.67
N_D	3064	3169	3169	3169	3169	3169
N_V	52	52	52	52	49	49
N_P	708	795	845	768	1747	2025

B_{ij} are the components of the anisotropic thermal vibrations (defined by $B_{ij}=8\pi^2\langle u_{ij}^2\rangle$, where u_{ij} is the mean-square amplitude of the vibration in direction ij), and B_{iso} is the refined isotropic thermal vibration parameter. In space group *Pbnm* the *X*2 and *X*3 positions are independent, whilst they are related by symmetry in the case of *Cmcm*. In the latter case the corresponding values are given for the *X*3 positions (and denoted by a symbol †), with $x_{X3}=x_{X2}-\frac{1}{2}$ and $y_{X3}=y_{X2}-\frac{1}{2}$. The weighted profile (WP) and profile (P) *R*-factors are given by

$$R_{WP}^2=\sum_{N_D}\frac{(I_{obs}-I_{calc})^2}{(\sigma I_{obs})^2}\Big/\sum_{N_D}\frac{(I_{obs})^2}{(\sigma I_{obs})^2}\quad\text{and}\quad R_P^2=\sum_{N_D}(I_{obs}-I_{calc})^2\Big/\sum_{N_D}(I_{obs})^2,$$

respectively, and the goodness-of-fit parameter χ^2 is given by

$$\chi^2=\sum_{N_D}\frac{(I_{obs}-I_{calc})^2}{(\sigma I_{obs})^2}\Big/(N_D-N_V).$$

The summations are made over the N_D data points used in the fit. I_{obs} and I_{calc} are the observed and calculated intensities, respectively, and σI_{obs} is the estimated standard deviation on I_{obs} derived from the counting statistics. N_V is the number of fitted variables and N_P is the number of Bragg peaks within the fitted data range. The values within parentheses represent the estimated standard deviations on the fitted parameters.

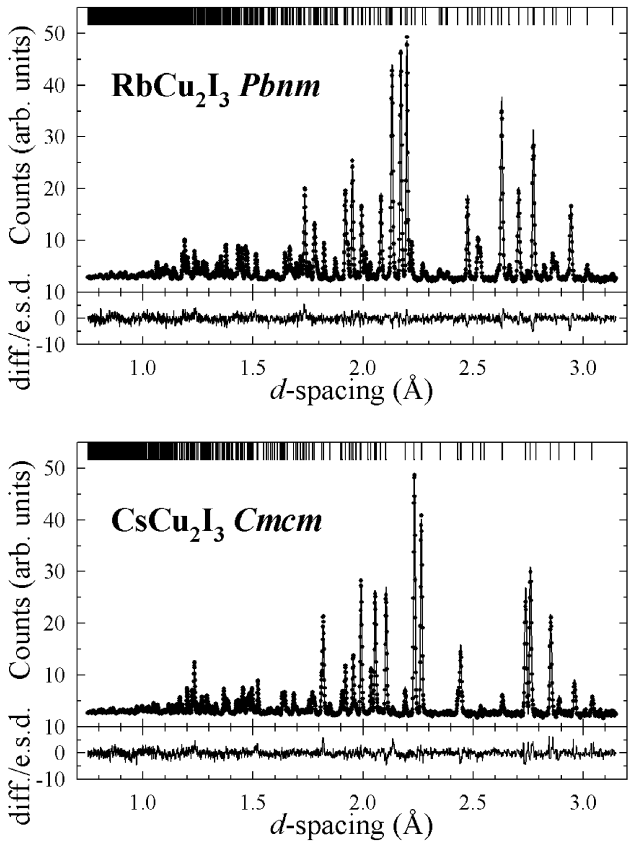

Fig. 12. The least-squares fit to the powder neutron diffraction data collected from $CsCu_2I_3$ (bottom) and $RbCu_2I_3$ (top) at ambient temperature. The dots are the experimental data points (with fitted background subtracted) and the solid line is the calculated profile using the parameters listed in Table 5. The lower trace shows the difference (measured minus calculated) divided by the estimated standard deviation on the experimental data points. The row of tick marks along the top of the figure denote the calculated positions of all the symmetry allowed Bragg reflections.

large anisotropic thermal vibrations and might be expected to undergo a transition from *Cmcm* symmetry to *Pbnm* at low temperatures. The least-squares fits for the two cases are illustrated in Fig. 12 for the representative examples of $RbCu_2I_3$ (*Pbnm*) and $CsCu_2I_3$ (*Cmcm*).

The tilting of the AX_4 tetrahedral chains causes the cavity occupied by the M cations to distort. In $CsCu_2I_3$ the Cs^+ are surrounded by 8 anions whilst in $RbCu_2I_3$ this cavity is distorted such that the Rb^+ are surrounded by a co-ordination shell which can be described as $7+2$. Taking $r_A + r_X$ as a crude measure of the size of the tetrahedra, then the ratio of the size of the M cations to the size of these polyhedra can be written as $r_M/(r_A + r_X)$. As expected, the rotation of the tetrahedral chains that lowers the symmetry from *Cmcm* to *Pbnm* only occurs when this factor is lowest, as the structural distortion allows anions to approach closer to the smaller M^+ cations.

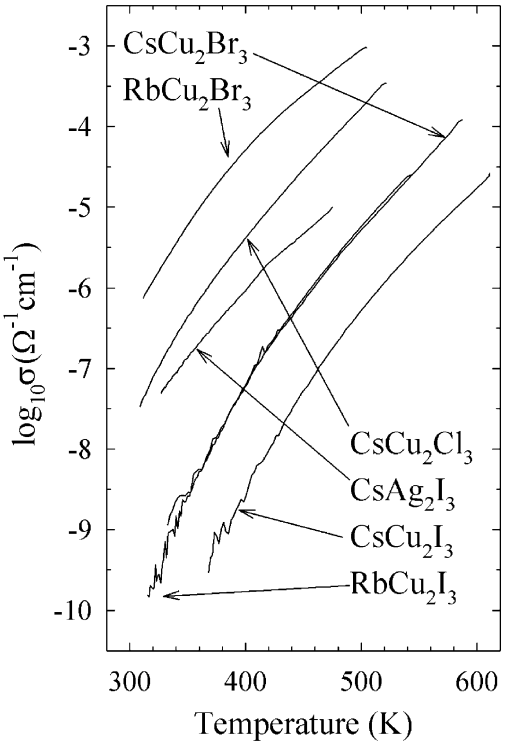

Fig. 13. The temperature variation of the ionic conductivity $\log_{10}\sigma$ of the six compounds of stoichiometry MA_2X_3. The apparent jitter in the data within the lower temperature region is due to the resistance of the sample approaching the upper limit of the measurement apparatus.

Fig. 13 illustrates the measured ionic conductivities of the six compounds of stoichiometry MA_2X_3. The two compounds which adopt *Pbnm* symmetry do not show conductivities significantly different to the other compounds and it appears that the structural distortion plays little or no role in the migration of ions. Interestingly, the conductivity increases in the sequences $RbCu_2I_3 \rightarrow RbCu_2Br_3$ and $CsCu_2I_3 \rightarrow CsCu_2Br_3 \rightarrow CsCu_2Cl_3$, indicating that the smaller anions promote Cu^+ migration. As noted previously, this is somewhat unexpected.

3.5. MA_4X_5 compounds

The three compounds $RbAg_4I_5$, KAg_4I_5 and KCu_4I_5 were originally identified in the 1960s [17–19] and their structural properties and ionic conductivities have been discussed in a previous paper [49]. $RbAg_4I_5$ and KAg_4I_5 have room temperature ionic conductivities of $\sigma = 0.21(6)$ and $0.08(5)\,\Omega^{-1}\,cm^{-1}$, respectively, which increase gradually on increasing temperature. KCu_4I_5 is only stable in the temperature range between 515(5) K and its melting point of 605 K, and its ionic conductivity is $\sigma = 0.61(8)\,\Omega^{-1}\,cm^{-1}$ at $T = 540$ K [49]. At lower temperatures KCu_4I_5 disproportionates into $KI + 4CuI$ and the ionic conductivity falls by over three orders of

magnitude. All three compounds are isostructural (space group $P4_132$) and the relationship between the crystal structure and the observed high ionic conductivity will be discussed in Section 4.3.

3.6. MA_9X_{10} compounds

The presence of phases of stoichiometry $CsCu_9Br_{10}$ and $CsCu_9I_{10}$ was first suggested by DTA and ionic conductivity measurements of the two binary phase diagrams [21]. Both were proposed to exist over a narrow range of temperature (563–579 K for $CsCu_9Br_{10}$ and 606–621 K for $CsCu_9I_{10}$) and both were reported to possess high values of ionic conductivity ($\sigma \sim 0.3\,\Omega^{-1}\,cm^{-1}$). The formation of these phases was observed as a sharp increase in σ and their upper limit of stability characterized by a change (decrease) in the slope of the σ versus temperature curve. A subsequent DSC study of the CuBr–CsBr system provided a slightly different observation, with the stoichiometry of the phase found to be closer to $CsCu_{19}Br_{20}$ and stable over a wider temperature range from 562 to 624 K [22].

Neutron diffraction data were collected for samples of $(CuBr)_{0.9}$–$(CsBr)_{0.1}$ and $(CuI)_{0.9}$–$(CsI)_{0.1}$ on increasing temperatures up to 633 and 693 K, respectively. In both cases the initial mixtures of CuX and CsX reacted slowly at $\sim$550 K on first heating to form a two-phase mixture of CuX and a small amount of $CsCu_2X_3$. No evidence of compounds of stoichiometries $CsCu_9X_{10}$ (or similar) were observed in either case, despite several heating and cooling cycles. Interestingly, the sequence of phase transitions observed within pure CuI on heating (zincblende (γ) $\rightarrow$ hexagonal (β) $\rightarrow$ fcc (α) [50]) is modified by the addition of CsI. In particular, the hexagonal β phase is not observed, presumably because a small amount of Cs^+ is incorporated into the CuI lattice and restricts the shearing of the two-dimensional close packed anion layers as the iodine sublattice transforms from fcc in the γ phase to hcp in the β phase. This observation has proved useful to probe the nature of the superionic transition within CuI and has been discussed in more detail elsewhere [51].

4. Discussion

4.1. Factors influencing superionic behavior

The key issue when considering the systematic behavior of the ternary phases present in the $(AX)_x$–$(MX)_{1-x}$ systems is the factors which influence the ionic conductivity. In Table 6 the ionic conductivities of the various compounds at 400 K are listed, together with the values of activation energy E_a derived by fitting the usual expression $\sigma = Ae^{-E_a/kT}$ to the experimental data presented in Figs. 3, 4, 6, 8 and 13. In the majority of cases, plots of $\log_{10}\sigma$ versus $1/T$ showed a single linear region extending over the entire measured temperature range. For a few samples, curvature of the plots occurred close to the upper temperature limit and the values of E_a were determined using only the linear portion. Complementary data for the MAg_4I_5 systems is also included in Table 6 [49], showing that these two compounds are the only phases observed to have high ionic conductivities at temperatures close to ambient. It is straightforward to demonstrate that this is not merely a consequence of the packing density of the immobile M^+ and X^- ions. Table 6 shows a calculation of the expression

$$F_V = 1 - \left(\sum_{N_M}\frac{4}{3}\pi r^3 + \sum_{N_X}\frac{4}{3}\pi r^3\right)/V_u,$$

where N_M and N_X are the numbers of M^+ and X^- ions within the unit cell, respectively, r is their radius [52] and V_u is the volume of the unit cell. This illustrates that the fraction F_V of 'empty' space available for the diffusing A^+ is, if anything, slightly higher in the case of the MX

Table 6
Values of the ionic conductivity measured at 400 K ($\sigma_{400\,K}$), the activation energy for A^+ diffusion (E_a), the fraction of 'free volume' within the unit cell (F_V) and the Phillips ionicity (f_i). The latter two properties are defined in Section 4.1. Corresponding values for the highly conducting compounds $RbAg_4I_5$ and KAg_4I_5 are also included for comparison [49,88]

Compound	$\sigma_{400\,K}$ ($\Omega^{-1}\,cm^{-1}$)	E_a (eV)	F_V	f_i
Cs_2AgCl_3	7.8×10^{-9}	0.29(1)	0.574	0.923
Rb_2AgBr_3	1.3×10^{-8}	0.27(1)	0.597	0.921
Cs_2AgBr_3	3.8×10^{-9}	0.32(2)	0.595	0.922
K_2AgI_3	6.5×10^{-8}	0.30(1)	0.670	0.890
Rb_2AgI_3	6.3×10^{-9}	0.28(1)	0.652	0.891
Cs_2AgI_3	2.8×10^{-8}	0.30(1)	0.644	0.892
K_2CuCl_3	1.1×10^{-7}	0.36(2)	0.616	0.884
K_2CuBr_3	9.5×10^{-8}	0.37(2)	0.645	0.880
Rb_2CuCl_3	5.0×10^{-9}	0.42(1)	0.598	0.885
Rb_2CuBr_3	7.8×10^{-9}	0.38(1)	0.625	0.883
$Cs_3Cu_2Cl_5$	2.1×10^{-7}	0.29(1)	0.601	0.872
$Cs_3Cu_2Br_5$	1.7×10^{-7}	0.30(1)	0.628	0.869
$Cs_3Cu_2I_5$	1.3×10^{-9}	0.41(1)	0.679	0.849
β-$CsAgCl_2$	2.4×10^{-9}	0.38(2)	0.601	0.906
β-$CsAgBr_2$	4.3×10^{-8}	0.41(1)	0.629	0.904
$CsCu_2Cl_3$	4.2×10^{-6}	0.26(2)	0.618	0.816
$CsCu_2Br_3$	6.5×10^{-8}	0.33(3)	0.659	0.809
$CsCu_2I_3$	2.8×10^{-9}	0.38(2)	0.736	0.779
$RbCu_2Br_3$	5.1×10^{-5}	0.22(1)	0.644	0.809
$RbCu_2I_3$	6.2×10^{-8}	0.34(3)	0.726	0.778
$CsAg_2I_3$	9.1×10^{-7}	0.21(2)	0.657	0.831
α-$RbAg_4I_5$	0.42	0.12(1) [88]	0.670	0.806
α-KAg_4I_5	0.18	0.12(1) [88]	0.674	0.806

The values within parentheses represent the estimated standard deviations on the fitted parameters.

rich compounds of stoichiometry M_2AX_3 than the superionic ones of stoichiometry MA_4X_5.

The binary AgX and CuX halides exhibit mixed ionic-covalent character in their bonding and this feature has been proposed to be a key factor in promoting superionic behavior [53,54]. Indeed, on the Phillips scale of ionicity [55] they straddle the so-called 'critical' value of $f_c = 0.785$ which separates compounds characterised by 4-fold ('covalent') and six-fold ('ionic') co-ordination of the unlike ions. Thus, CuCl ($f = 0.746$), CuBr ($f = 0.735$) and CuI ($f = 0.692$) all crystallize in the cubic zincblende structure and AgI ($f = 0.770$) usually exists as a two-phase mixture of zincblende and its hexagonal equivalent, wurtzite. In contrast to this tetrahedral co-ordination, the cations are octahedrally co-ordinated to anions in the cubic rocksalt structured AgCl ($f = 0.856$) and AgBr ($f = 0.850$). The suggestion that the ionicity of the ternary compounds (calculated as the composition weighted average of the values given for the binary AX and MX compounds [55]) can be used to identify high conductivity phases [21] does not bear close scrutiny. As illustrated in Table 6, the proposed critical upper limiting value for superionic behavior of $f_i = 0.809$ is consistent with the behavior of the three MA_4X_5 compounds. However, it also implies that $CsCu_2I_3$ ($f_i = 0.779$) and $RbCu_2I_3$ ($f_i = 0.778$) should be highly conducting phases, but this is not so (see Fig. 13).

4.2. Favored M^+ and A^+ co-ordinations

With the exception of the 3-fold co-ordination demonstrated by one of the Cu^+ sites (Cu1) within the three $Cs_3Cu_2X_5$ compounds, the Ag^+ and Cu^+ reside in tetrahedrally co-ordinated sites in all the ternary derivatives of CuCl, CuBr, CuI and AgI. Ignoring slight distortions, the co-ordination mirrors that adopted within the corresponding binary halides and represents the most common environment adopted in their wider family of ternary derivatives.[1] By contrast, Ag^+ does not achieve its 'ideal' 6-fold co-ordination within the ternary derivatives of AgCl and AgBr to mimic the situation observed in the rocksalt structured binary parent compounds. Instead, Ag^+ is either tetrahedrally co-ordinated or 5-fold co-ordinated to anions, the latter within trigonal bipyramidal or square pyramidal environments within the β and α phases of the $CsAgX_2$ compounds (see Fig. 9).

As expected, the larger size of the M^+ cations is reflected in their higher anion co-ordination numbers. The six binary compounds KX and RbX all adopt the octahedrally co-ordinated rocksalt structure. However, within the ternary compounds this arrangement is only observed in a highly distorted form in the MA_4X_5 compounds, with two opposite triangular faces rotated with respect to one another [49]. Instead, the K^+ and Rb^+ generally reside at the centers of rather irregular polyhedra formed by 7 anions. One exception is $RbCu_2Br_3$, in which the Rb^+ are 8-fold co-ordinated, though the co-ordination polyhedron is a distorted square antiprism of Br^-, rather than the regular cube found in the CsCl structured CsX binary compounds. Within the ternary compounds Cs^+ is observed in both irregular 7-fold co-ordination and square antiprism (8-fold) environments.

4.3. Influence of the crystal structure on the superionic properties

The extensive diffusion of Ag^+ within the highly conducting compound $RbAg_4I_5$ has been attributed to the specific nature of the anion sublattice [18,19,49]. The I^- adopt an arrangement similar to that observed within the β phase of elemental Mn, with the Rb^+ occupying distorted octahedral cavities. Within this structure there are a total of 72 suitable interstices which could accommodate the $16 \times Ag^+$ in each unit cell, formed by 5 symmetry independent sites with 4- or 5-fold co-ordination. However, neutron diffraction studies show that the Ag^+ predominantly occupy only two sets of sites with roughly tetrahedral co-ordination [49]. The cations diffuse along one-dimensional channels parallel to the $\langle 001 \rangle$ axes formed by face-sharing strings of these anion tetrahedra, with some hopping between adjacent channels.

A similar discussion for the various ternary structures will now be given, using Rb_2AgI_3, Cs_2AgI_3, $Cs_3Cu_2I_5$, $AgCsBr_2$ and $CsCu_2I_3$ as representative examples of the five major ternary structure types adopted in the $(AgX)_x$–$(MX)_{1-x}$ and $(CuX)_x$–$(MX)_{1-x}$ systems (type-I and type-II for M_2AX_3; $M_3A_2X_5$, MAX_2 and MA_2X_3, respectively).

The anion sublattice within Rb_2AgI_3 (structure type I, space group *Pnma*) comprises a structural array formed by three symmetry independent I^- sites, all in 4(c) x, 1/4, z positions (see Table 2). This sublattice contains a number of relatively large voids, with triangular prisms centered on 4(c) sites with $x \approx 0.371$ and $z \approx 0.897$ and two further sets of distorted triangular prisms around 4(c) sites with $x \approx 0.578$, $z \approx 0.792$ and $x \approx 0.258$, $z \approx 0.454$. The latter have a seventh I^- situated outside one of the square faces and are occupied by the Rb1 and Rb2 cations, respectively. There are also three sets of tetrahedral cavities, all centered on 4(c) sites. The first is filled by Ag^+ with $x \approx 0.131$, $z \approx 0.136$, whilst the two empty tetrahedra are labelled $A1$ and $A2$ and located at $x \approx 0.464$, $z \approx 0.317$ and $x \approx 0.101$, $z \approx 0.035$, respectively. As illustrated in Fig. 2, each AgI_4 tetrahedron shares two corners with other AgI_4 units, forming strings parallel to the [010] axis. The AgI_4 tetrahedra share one

[1] One exception being the octahedral environment of Ag^+ within Tl_2AgI_3 [56].

face with an empty $A1I_4$ tetrahedron and another with an empty $A2I_4$ tetrahedron. However, the $A2I_4$ units are linked only by a common edge and there are no long-range pathways between tetrahedrally co-ordinated sites which share faces.

Cs_2AgI_3 (structure type II, space group *Pnma*) also possesses three symmetry independent I^- sites. The anion sublattice contains the same number of distorted (monocapped) trigonal prisms and tetrahedral interstices as Rb_2AgI_3, with the two Cs^+ sites in 4(*c*) x, 1/4, z positions with (on geometric grounds) $x_{Cs1}\approx 0.18$, $z_{Cs1}\approx 0.478$ and $x_{Cs2}\approx 0.516$, $z_{Cs2}\approx 0.676$. The Ag^+ are located in one of the sets of tetrahedral voids (4(*c*) with $x\approx 0.255$ and $z\approx 0.197$). The empty tetrahedra are also in 4(*c*) sites, *A*1 being centered at $x\approx 0.109$ and $z\approx 0.246$ and *A*2 at $x\approx 0.435$ and $z\approx 0.929$. In common with the closely related structure type I, the AgI_4 tetrahedra form infinite corner-sharing strings parallel to the [010] axis and there are no long-range pathways of connected face-sharing tetrahedra. The filled AgI_4 units share one face with an $A1I_4$ tetrahedron, which only shares an edge with an empty $A2I_4$ tetrahedron.

Similar comments also apply to $Cs_3Cu_2I_5$ (space group *Pnma*). The anion sublattice comprises four symmetry independent I^- sites and contains two large interstices in 4(*c*) x, 1/4, z positions at $x\approx 0.591$, $z\approx 0.553$ and 8(*c*) x, y, z sites at $x\approx 0.054$, $y\approx 0.995$, $z\approx 0.681$. These are the sites occupied by Cs1 and Cs2, respectively. There are three sets of tetrahedral interstices, which are all in 4(*c*) sites. These are $x\approx 0.228$, $z\approx 0.538$ (occupied by Cu2); $x\approx 0.381$, $z\approx 0.328$ (empty, labelled *A*1) and $x\approx 0.175$, $z\approx 0.393$ (empty, labelled *A*2). The *A*1 and *A*2 centered tetrahedra share a face with each other and the CuI positions lie close to the center of the common triangular face. The $Cu2I_4$ tetrahedra share a common face with an $A2I_4$ unit but are isolated from other filled $Cu2I_4$ tetrahedra.

Within the β phase of $CsAgBr_2$ (space group *Cmcm*) the two sets of anions in 4(*c*) 0, y, 1/4 sites form a rather irregular sublattice. This array contains slightly distorted cubic interstices, situated in 4(*c*) sites with $y\approx 0.578$ and occupied by Cs^+. There are also unoccupied square planar interstices centered on 4(*b*) 0, 1/2, 0 positions and distorted tetrahedra centered on 8(*f*) 0, y, z sites with $y\approx 0.796$ and $z\sim 0.211$. Pairs of these tetrahedra share a common face, such that their centers are only a distance $(1/2-2z)c\approx 0.5$ Å apart along the [001] direction. The Ag^+ reside at the midpoint between these sites, in 4(*c*) sites with $y_{Ag}\approx 0.796$, and are thus surrounded by a distorted trigonal bipyramid of anions.[2] The $AgBr_5$ units share only common edges and their linkage is unchanged above the $\beta\rightarrow\alpha$ transition observed on increasing temperature (see Section 3.3).

The anions within $CsCu_2I_3$ (space group *Cmcm*) occupy two symmetry independent sites. Together these form a relatively close packed anion array containing large interstices centered on 4(*c*) 0, y, 1/4 sites with $y_{Cs}\approx 0.685$ which are occupied by Cs^+. The Cs^+ are surrounded by $6\times I^-$ at the corners of a trigonal prism with additional anions located outside two of the lateral faces. There are also two sets of 4-fold co-ordinated sites, formed by anion tetrahedra centered on 8(*e*) x, 0, 0 positions with $x\approx 0.860$ and by square planar arrangements of four I^- around the 4(*b*) 0, 1/2, 0 positions. All of the former are occupied by Cu^+, such that the CuI_4 tetrahedra share common edges to form double chains in the direction of the *c*-axis, as illustrated in Fig. 11.

Within the ternary $(AX)_x$–$(MX)_{1-x}$ compounds, infinite strings of face-sharing anion tetrahedra are only a feature of the structure of the three compounds of stoichiometry M_4AX_5, suggesting their presence is a necessary condition for high ionic conductivity. This hypothesis has been put forward previously, and is based on the observation that the M^+ cations are invariably bigger than the A^+ (see Ref. [1] and references therein). By placing a greater 'demand' on the available anions, the X^- sublattice is forced into a greater degree of face-sharing of the tetrahedra [57]. If x is less than ~ 0.8 then the more numerous M^+ ions essentially 'use up' the excess co-ordination capacity. The resultant structures contain, at most, only pairs of face-sharing tetrahedra and are unfavorable for long-range A^+ diffusion [1]. Similar arguments imply that large M^+ species will hinder superionic conduction and are consistent with the absence of a highly conducting Ag_4CsI_5 phase [17] and with the need for smaller concentrations of M^+ to form superionic $(AgX)_x$–$(MX)_{1-x}$ compounds containing larger species such as $(CH_3)_4N$, $(CH_3)_2(C_2H_5)_2$ and $(C_2H_5)_4N$ [58].

Whilst the intuitive discussion given in the previous paragraph is consistent with the experimental data presented in this paper, the real situation is not quite so simple. For example, neutron diffraction studies show that only a subset of the face-shared tetrahedral pathways play a role in the Ag^+ diffusion process within Ag_4RbI_5 [49]. Similarly, diffusion via common tetrahedral faces is not the only diffusion mechanism observed within Ag^+ and Cu^+ superionics. This is illustrated by α-CuI, in which diffusion of Cu^+ between the tetrahedrally co-ordinated interstices has been shown to occur in $\langle 001\rangle$ directions via a shared tetrahedral *edge* [59–62].

There are two simulation techniques which can, in principle, be used to 'predict' whether a given compound will display superionic behavior. The first of these is

[2] Given the proximity of the tetrahedral sites to the reported 5-fold co-ordinated one, alternative fits placing the Ag^+ on 8(*f*) sites with a mean occupancy of 1/2 were attempted. However, these did not provide stable refinements.

the molecular dynamics (MD) method, which has been widely used to study ionic diffusion processes within the binary Ag^+ and Cu^+ halides (see, for example, Refs. [51,59–70]). Its major drawbacks lie in the high computational demands and the need for reliable (and transferable) interionic potentials derived by empirical or ab-initio means. The second approach is the bond valence difference method. This technique has recently been used to probe the plausible sites occupied by diffusing ions and, specifically, to investigate the likely conduction pathways for the diffusing ions within both crystalline and amorphous superionics [71–80]. The next paper in this series will assess the reliability of this approach to probe the structural properties and ionic conduction mechanisms of the various Ag^+ and Cu^+ ternary halides and compare this method with the more commonly used MD method. It is, therefore, appropriate to derive the bond valence parameters for the Ag–X and Cu–X bonds, using the new crystallographic data reported in this paper and that published within the literature. This process is described in Appendix A.

5. Conclusions

A comprehensive study of the structural properties and ionic conductivities of the ternary compounds present within the $(AgX)_x$–$(MX)_{1-x}$ and $(CuX)_x$–$(MX)_{1-x}$ systems confirm that the only highly conducting phases are the three compounds $RbAg_4I_5$, KAg_4I_5 and KCu_4I_5. The presence of supernumerary tetrahedral cavities linked by low energy diffusion pathways (via shared tetrahedral faces) has been used to explain the high ionic conductivities shown by these MA_4X_5 compounds [49], as it has in the binary bcc structured α-AgI phase [5]. To investigate further the relationship between the crystal structures and diffusion properties within these compounds a forthcoming paper will exploit computational techniques, based on bond valence and MD methods, but validated with reference to the experimental data presented here.

Acknowledgments

The work presented in this paper forms part of a wider project investigating the structural properties of superionic conductors funded by the Engineering and Physical Sciences Research Council (reference GR/M38711). One of the authors (PB) wishes to thank the Swedish Research Council for financial support. We are very grateful to D.A. Keen and J. Dreyer for their assistance with the high temperature neutron diffraction measurements at ISIS and to J. Grins and M. Brunelli for collecting X-ray diffraction data at the ESRF, Grenoble. We wish to acknowledge the use of the EPSRC's Chemical Database Service at Daresbury.

Appendix A

A.1. Overview of the bond valence method

The use of bond valence methods to study the ionic distributions within superionic compounds was demonstrated during the 1980s for α-AgI [81] and CaF_2 [82]. The method is based on the observation that, for most inorganic compounds, the formal valence V_i of an ion i comprises the sum of bond valences (bond strengths) s_{ij} to all the ions j of opposite charge within the first coordination shell,

$$\sum_j s_{ij} \cong V_i. \tag{A.1}$$

Two commonly used relationships between the bond valence s_{ij} and the bond length r_{ij} are

$$s_{ij} = \left(r_{ij}/r_0\right)^{-N} \tag{A.2}$$

and

$$s_{ij} = \mathrm{e}^{(r_0 - r_{ij})/B}, \tag{A.3}$$

where r_0, N and B are empirically determined parameters. In this paper we use Eq. (A.3), which is often preferred to Eq. (A.2) because the value of B varies little for bonds between similar ions (unlike N in Eq. (A.2)). Indeed, a value $B = 0.37$ Å has been shown to be consistent with most bonds between pairs of ions [83], though the validity of this assumption has recently been questioned [84]. Clearly, the accuracy of any structural or chemical information extracted using the bond-valence method is dependent on the reliability of the parameters r_0 and B in Eq. (A.3). Several attempts to derive bond valence parameters for various ion pairs have been made, based on the appropriate anion and cation radii and with corrections for electronegativity or position within the periodic table [83,85]. However, whilst these methods are adequate to predict approximate bond lengths or to check the reliability of a proposed structural model, a detailed interpretation of a crystal structure is best performed using values obtained from accurately determined structures of closely related compounds [86]. In practice, this requires crystallographic details from a number (ideally >10) of good quality structure refinements. Unfortunately, this requirement is generally only met by oxides and a small number of sulfides and fluorides.

As a consequence, the structural data presented here has been used, together with that published previously within the literature, to determine improved values of the bond valence parameters for Ag–X and Cu–X bonds.

Table 7
Summary of the bond valence parameters r_0 and B determined in the course of this work

Bond		N_{comp}	N_{cat}	r_0 (Å) [86]	r_0 (Å) ($B = 0.37$ Å)	r_0 (Å)	B (Å)
Ag–X	Ag–Cl	8	8	2.09	2.085	1.908	0.476
	Ag–Br	6	6	2.22	2.196	2.024	
	Ag–I	11	13	2.38	2.338	2.184	
Cu–X	Cu–Cl	12	15	1.85	1.846	1.692	
	Cu–Br	11	12	1.99	1.969	1.820	
	Cu–I	9	10	2.16	2.128	1.979	

Values for r_0 obtained with B varied and fixed at a value of 0.37 Å are given, together with those estimated previously on the basis of a smaller number of structural studies [86]. N_{comp} and N_{cat} are the number of compounds and the number of cation sites used in the fitting procedure.

A.2. Derivation of bond valence parameters for A–X bonds

The initial stage in the process of determining the bond valence parameters r_0 and B for the $6 \times A$–X bonds is to assemble a set of suitable, reliable crystal structures using the ICSD database [43]. The criteria used to select these are (i) find all those structures containing the relevant monovalent cations (Ag^+ or Cu^+) and one (or more) of the relevant halide ions (Cl^-, Br^- and I^-); (ii) accept only those refinements with a weighted R-factor (R_{WP}) reported to be $\leqslant 10\%$; (iii) accept only those structures refined under ambient conditions of pressure and temperature and (iv) reject any structures containing disordered anions and any cation sites which have fractional occupancies.

Traditionally, the bond valence sums for cations obtained via Eq. (A.3) considered only those anions within the first co-ordination shell. However, it has recently been shown that the quality of the structural information (especially when probing ionic diffusion mechanisms) can be improved by performing the summation to greater distances [84]. In practice, convergence is achieved at a distance $r_{max} = 10$ Å. A drawback of this enhancement is, of course, that a number of compounds containing Cl^-, Br^- or I^- and other anions species (such as O^{2-}) cannot be included, even if the latter lie outside the cation's immediate environment. This process provided crystallographic data for a total of 38 compounds, to be added to that for the 21 systems reported in this paper.

Determination of the bond valence parameters minimized the function

$$Y = \sum_{i=1}^{N_{cations}} \left(V_i - \sum_{j=1}^{N_{anions}} s_{ij} \right)^2,$$

where V_i is the ionic valence ($+1$ in all the cases considered here). The resultant values of

$$\left(V_i - \sum_{j=1}^{N_{anions}} s_{ij} \right)$$

for each cation i were inspected and a small number of compounds were rejected, presumably due to an error in the original paper or a typographical mistake in the database. Several of the structures considered possess cations occupying more than one symmetry independent position and the total number of cation environments used in the minimization totalled 64. The number for each bond type is listed in Table 7.

A minimum value of Y (0.235) was determined by varying the values of r_0 for the six A-X pairs at the same time, since this simultaneous approach allows the small number of mixed halide compounds (such as Cu_2CsCl_2I [87]) to be included. The values obtained with B fixed at a value of 0.37 Å are listed in Table 7. A subsequent minimization of Y to 0.163 was obtained by allowing B to vary. This process gave a value $B = 0.476$.[3] Owing to the limited number of cation environments available it was not possible to vary B independently for each A–X pair.

References

[1] S. Chandra, Superionic Solids: Principles and Applications, North-Holland Publishing Company, Amsterdam, 1981.
[2] J.B. Boyce, T.M. Hayes, J.C. Mikkelsen Jr., Phys. Rev. B 23 (1981) 2876–2896.
[3] D.A. Keen, J. Phys.: Condens. Matter 14 (2002) R819–R857.
[4] A.F. Wright, B.E.F. Fender, J. Phys. C: Solid State Phys. 10 (1977) 2261–2267.
[5] V.M. Nield, D.A. Keen, W. Hayes, R.L. McGreevy, Solid State Ionics 66 (1993) 247–258.
[6] W. Bührer, W. Hälg, Electrochem. Acta 22 (1977) 701–704.
[7] S. Hull, D.A. Keen, W. Hayes, N.J.G. Gardner, J. Phys.: Condens. Matter 10 (1998) 10941–10954.
[8] V.M. Nield, R.L. McGreevy, D.A. Keen, W. Hayes, Physica B 202 (1994) 159–166.
[9] S. Hull, D.A. Keen, J. Phys.: Condens. Matter 8 (1996) 6191–6198.
[10] D.A. Keen, S. Hull, W. Hayes, N.J.G. Gardner, Phys. Rev. Lett. 77 (1996) 4914–4917.

[3] An empirical relationship between the value of B and differences in the 'softness' of the anion and cations that form the bond has been described elsewhere [84].

[11] S. Hull, D.A. Keen, J. Phys.: Condens. Matter 12 (2000) 3751–3765.
[12] S. Hull, D.A. Keen, J. Phys.: Condens. Matter 13 (2001) 5597–5610.
[13] S. Hull, D.A. Keen, N.J.G. Gardner, W. Hayes, J. Phys.: Condens. Matter 13 (2001) 2295–2316.
[14] S. Hull, D.A. Keen, P. Berastegui, Solid State Ionics 147 (2002) 97–106.
[15] S. Hull, D.A. Keen, P. Berastegui, J. Phys.: Condens. Matter 14 (2002) 13579–13596.
[16] J.N. Bradley, P.D. Greene, Trans. Faraday Soc. 62 (1966) 2069–2075.
[17] J.N. Bradley, P.D. Greene, Trans. Faraday Soc. 63 (1967) 424–430.
[18] J.N. Bradley, P.D. Greene, Trans. Faraday Soc. 63 (1967) 2516–2521.
[19] S. Geller, Science 157 (1967) 310–312.
[20] S. Geller, J.R. Akridge, S.A. Wilber, Phys. Rev. B 19 (1979) 5396–5402.
[21] O. Yamamoto, in: B. Scrosati, A. Magistris, C.M. Mori, G. Mariotto (Eds.), Fast-Ion Transport in Solids, NATO ASI Series E, Vol. 250, Kluwer Academic Publishers, Dordrecht, 1993, pp. 203–211.
[22] A. Wojakowska, E. Krzyzak, A. Wojakowski, Thermochim. Acta 344 (2000) 55–59.
[23] N.J.G. Gardner, S. Hull, D.A. Keen, P. Berastegui, Rutherford Appleton Laboratory Internal Report, RAL-TR-1998-032, 1998.
[24] S. Hull, R.I. Smith, W.I.F. David, A.C. Hannon, J. Mayers, R. Cywinski, Physica B 180–181 (1992) 1000–1002.
[25] P.E. Werner, L. Eriksson, M. Westdahl, J. Appl. Crystallogr. 18 (1985) 367–370.
[26] A.C. Larson, R.B. Von Dreele, Los Alamos National Laboratory Report, LAUR 86-748, 1985.
[27] A.J.C. Wilson (Ed.), International Tables for Crystallography: Volume C, Kluwer Academic Publisher, Dordrecht, 1995.
[28] C. Hasselgren, S. Jagner, Acta Crystallogr. C 55 (1999) 1208–1210.
[29] C. Brink, C.H. MacGillavry, Acta Crystallogr. 2 (1949) 158–163.
[30] C. Brink, H.A.S. Kroese, Acta Crystallogr. 5 (1952) 433–436.
[31] M.M. Thackeray, J. Coetzer, Acta Crystallogr. B 31 (1975) 2339–2340.
[32] I.D. Brown, H.E. Howard-Lock, M. Natarajan, Can. J. Chem. 55 (1977) 1511–1514.
[33] Y. Suenaga, M. Maekawa, T. Kuroda-Sowa, M. Munakata, Anal. Sci. 13 (1997) 647–649.
[34] R. Kanno, Y. Takeda, Y. Masuyama, O. Yamamoto, T. Takahashi, Solid State Ionics 11 (1983) 221–226.
[35] R.M. Biefield, Mater. Res. Bull. 10 (1975) 1151–1156.
[36] C. Brink, A.E. van Arkel, Acta Crystallogr. 5 (1952) 506–510.
[37] M. Hoyer, H. Hartl, Z. Anorg. Allg. Chem. 598 (1991) 151–162.
[38] C.B. Shoemaker, Z. Kristallogr. 137 (1973) 225–239.
[39] K.P. Bigalke, A. Hans, H. Hartl, Z. Anorg. Allg. Chem. 563 (1988) 96–104.
[40] B.M. Mykhalichko, V.N. Davydov, L.G. Akselrud, Z. Neorg. Khim. 42 (1997) 1125–1127.
[41] H.-C. Gaebell, G. Meyer, R. Hoppe, Z. Anorg. Allg. Chem. 497 (1983) 199–205.
[42] H.-C. Gaebell, G. Meyer, Z. Anorg. Allg. Chem. 513 (1984) 15–21.
[43] D.A. Fletcher, R.F. McMeeking, D.J. Parkin, Chem. Inf. Comput. Sci. 36 (1996) 746–749.
[44] H.-C. Gaebell, G. Meyer, R. Hoppe, Z. Anorg. Allg. Chem. 498 (1983) 94–98.
[45] C. Brink, N.F. Binnendijk, J. van de Linde, Acta Crystallogr. 7 (1954) 176–180.
[46] R.S. Pettigrosso, J.C. Bazán, M.E.F. de Rapp, Mater. Lett. 29 (1996) 81–85.
[47] G. Meyer, Z. Anorg. Allg. Chem. 515 (1984) 127–132.
[48] N. Jounini, L. Guen, M. Tournoux, Rev. Chim. Minér. 17 (1980) 486–491.
[49] S. Hull, D.A. Keen, D.S. Sivia, P. Berastegui, J. Solid State Chem. 165 (2002) 363–371.
[50] D.A. Keen, S. Hull, J. Phys.: Condens. Matter 7 (1995) 5793–5804.
[51] D.A. Keen, S. Hull, A.C. Barnes, P. Berastegui, W.A. Crichton, P.A. Madden, M.G. Tucker, M. Wilson, Phys. Rev. B 68 (2003) art. 014117.
[52] R.D. Shannon, Acta Crystallogr. A 32 (1976) 751–767.
[53] M. Aniya, Solid State Ionics 50 (1992) 125–129.
[54] M. Aniya, Solid State Ionics 70–71 (1994) 673–677.
[55] J.C. Phillips, Rev. Mod. Phys. 42 (1970) 317–356.
[56] M. Hoyer, H. Hartl, Z. Anorg. Allg. Chem. 622 (1996) 308–312.
[57] D.O. Raleigh, in: M. Kleitz, J. Dupuy (Eds.), Electrode Processes in Solid State Ionics, D. Reidel Publishing Co., Holland, 1976.
[58] B.B. Owens, in: C.W. Tobias (Ed.), Advances in Electrochemistry and Electrochemical Engineering, Vol. 8, Wiley, New York, 1971.
[59] J.X.M. Zheng-Johansson, I. Ebbsjö, R.L. McGreevy, Solid State Ionics 82 (1995) 115–122.
[60] J.X.M. Zheng-Johansson, R.L. McGreevy, Solid State Ionics 83 (1996) 35–48.
[61] R.L. McGreevy, J.X.M. Zheng-Johansson, I. Ebbsjö, Physica B 226 (1996) 107–112.
[62] R.L. McGreevy, J.X.M. Zheng-Johansson, Solid State Ionics 95 (1997) 215–220.
[63] P. Vashishta, A. Rahman, Phys. Rev. Lett. 40 (1978) 1337–1340.
[64] M. Parrinello, A. Rahman, P. Vashishta, Phys. Rev. Lett. 50 (1983) 1073–1076.
[65] P. Vashishta, I. Ebbsjö, R. Dejus, K. Sköld, J. Phys. C: Solid State Phys. 18 (1985) L291–L296.
[66] J.L. Tallon, Phys. Rev. B 38 (1988) 9069–9079.
[67] C.A. Rains, J.R. Ray, P. Vashishta, Phys. Rev. B 44 (1991) 9228–9239.
[68] K. O'Sullivan, G. Chiarotti, P.A. Madden, Phys. Rev. B 43 (1991) 13536–13548.
[69] P.A. Madden, K.F. O'Sullivan, G. Chiarotti, Phys. Rev. B 45 (1992) 10206–10212.
[70] S. Hull, D.A. Keen, D.S. Sivia, P.A. Madden, M. Wilson, J. Phys.: Condens. Matter 14 (2002) L9–L17.
[71] D. Mazza, S. Ronchetti, O. Bohnke, H. Duroy, J.L. Fourquet, Solid State Ionics 149 (2002) 81–88.
[72] S. Adams, J. Swenson, Phys. Chem. Chem. Phys. 4 (2002) 3179–3184.
[73] J. Swenson, S. Adams, Phys. Rev. B 6402 (2001) art. 024204.
[74] D. Mazza, J. Solid State Chem. 156 (2001) 154–160.
[75] S. Adams, J. Swenson, Phys. Rev. B 6305 (2001) art. 054201.
[76] S. Adams, Solid State Ionics 136 (2000) 1351–1361.
[77] J.S. Lee, S. Adams, J. Maier, J. Phys. Chem. Solids 61 (2000) 1607–1622.
[78] S. Adams, J. Swenson, Phys. Rev. Lett. 84 (2000) 4144–4147.
[79] S. Adams, A. Preusser, Acta Crystallogr. C 55 (1999) 1741–1743.
[80] S. Adams, J. Maier, Solid State Ionics 105 (1998) 67–74.
[81] J.D. Garrett, J.E. Greedan, R. Faggiani, S. Carbotte, I.D. Brown, J. Solid State Chem. 42 (1982) 183–190.
[82] I.D. Brown, Solid State Ionics 31 (1988) 203–208.
[83] I.D. Brown, D. Alternatt, Acta Crystallogr. B 41 (1985) 244–247.
[84] S. Adams, Acta Crystallogr. B 57 (2001) 278–287.
[85] M. O'Keeffe, N.E. Brese, J. Am. Chem. Soc. 113 (1991) 3226–3229.
[86] N.E. Brese, M. O'Keeffe, Acta Crystallogr. B 47 (1991) 192–197.
[87] S. Geller, J.M. Gaines, J. Solid State Chem. 59 (1985) 116–122.
[88] H. Looser, M. Mali, J. Roos, D. Brinkman, Solid State Ionics 9–10 (1983) 1237–1240.